MODELING OF AN AUTOTHERMAL HEAT-INTEGRATED WALL REACTOR FOR SIMULATION OF HYDROGEN PRODUCTION FOR FUEL CELL APPLICATIONS

by

Cihan Banu Biçici

B.S. in Mechanical Engineering, Boğaziçi University, 1999

Submitted to the Institute for Graduate Studies in
Science and Engineering in partial fulfillment of
the requirements for the degree of
Master of Science

Graduate Programs in Mechanical Engineering
Boğaziçi University
2005

ACKNOWLEDGEMENTS

This thesis was only made possible through the help and support of many people. Foremost, I would like to express my truthful gratitude to my thesis supervisor, Assist. Prof. Hasan Bedir for his guidance and trust in me. I would like to express my great appreciations for Assoc. Prof. Ecder and Assoc. Prof. Aksoylu for their valuable support and for sharing their scientific background with me. Cordial thanks to Prof. Günay Anlaş for his support and encouragement. I wish to thank Caner Kuzgunkaya for his everlasting understanding and patience. Very special thanks to Ekin Ozan Yener for his moral support and true friendship. Finally, I must certainly thank my mother for her years of patience, encouragement, and giving me confidence in all my endeavors.

ABSTRACT

MODELING OF AN AUTOTHERMAL HEAT-INTEGRATED WALL REACTOR FOR SIMULATION OF HYDROGEN PRODUCTION FOR FUEL CELL APPLICATIONS

An autothermal, heat integrated wall reactor model for hydrogen production for vehicular fuel cell applications is investigated using computer-based simulation techniques. The two dimensional reactor model is based on a hollow cylindrical tube enclosed in a bigger one, where different catalysts for exothermic partial oxidation and endothermic steam reforming reactions are deposited on the inside and outside surfaces of the tube. The reaction system is developed for catalytic conversion of methane with one step chemical kinetics. Reactor operation at different feed ratios and with different catalyst configurations is analyzed under steady state conditions. Results show that reactor efficiency is higher when the catalysts are placed closer as well as at high air-to-fuel and water-to-fuel ratios.

ÖZET

YAKIT PİLİ UYGULAMALARINDA HİDROJEN ÜRETİMİ BENZETİMİ İÇİN OTOTERMAL, DUVAR-ISI ENTEGRASYONLU REAKTÖR MODELLEMESİ

Taşıtlarda yakıt pili uygulamaları için hidrojen üretimine yönelik ototermal, duvar-ısı entegrasyonlu bir reaktör modeli bilgisayar destekli benzetim yöntemiyle incelenmiştir. İki boyutlu reaktör modeli, iç ve dış yüzeylerinde ekzotermik kısmi oksidasyon ve endotermik buharlı reformlama reaksiyonları için farklı katalizörler kaplanmış ve daha büyük bir silindirin içine kapatılmış silindirik bir tüpten oluşur. Reaksiyon sistemi, tek aşamalı kimyasal kinetiklere dayalı katalitik metan dönüşümü için oluşturulmuştur. Reaktörün denge durumundaki çalışması, farklı besleme karışımları ve katalizör konfigürasyonları için incelenmiştir. Sonuçlar, reaktör veriminin katalizörlerin birbirine yakın olduğu durumlar ve yüksek hava-yakıt ve buhar-yakıt oranları için daha fazla olduğunu göstermiştir.

TABLE OF CONTENTS

LIST OF FIGURES

LIST OF TABLES

LIST OF SYMBOLS/ABBREVIATIONS

T	Temperature
$\dot{r}_k'''$	Net rate of production of species k mass per unit volume
$\dot{r}_{k,s}'''$	Net rate of production of species k mass per unit surface
D_{km}	Diffusivity of species k into the mixture
X_k	Mole fraction of species k in the mixture
Y_k	Mass fraction of species k in the mixture
Le_k	Lewis number of species k
$\bar{M}$	Mixture molecular weight
$c_{p,k}$	Heat capacity of species k
h_k	Enthalpy pf species k
R	Universal gas constant
P	Pressure
P_k	Partial pressure of species k in the mixture
$cat\,w_j$	Catalyst surface coverage active for reaction j
k_j	Kinetic rate constant for reaction j
K_k	Adsorption coefficient for species k
E_j	Activation energy for reaction j
$\vec{\boldsymbol{m}}''$	Mass Flux vector
$\vec{\boldsymbol{n}}$	Unit normal vector
$\vec{\boldsymbol{u}}$	Bulk fluid velocity vector
$\vec{\boldsymbol{v}}_{\mathrm{k}}$	Diffusion velocity vector for species k in the mixture
$\vec{\boldsymbol{j}}_{\mathrm{k}}$	Diffusive mass flux vector
$\vec{\boldsymbol{q}}''$	Heat flux vector

β	Stretching parameter
ρ_k	Density of species k
λ_k	Conductivity of species k
λ_g	Conductivity of gas mixture
λ_s	Conductivity of solid
η_1	Effectiveness factor for reaction j

1. INTRODUCTION

The PEMFC requires hydrogen to operate, but since hydrogen gas is difficult to store and transport, it should be generated close to the final user. As a result, attention has been focused on the on-board conversion of more readily available hydrocarbon fuels to hydrogen in a device called fuel processor.

A fuel processor is a chemical device which converts hydrocarbon fuels to hydrogen. The fuels include petroleum-derived liquids, petroleum-derived gases, such as methane and propane, and other fuel such as methanol and ethanol.

In steam reforming process, steam reacts with the fuel in the presence of a catalyst to produce hydrogen, carbon monoxide, and carbon dioxide. The primary SR reaction is strongly endothermic, and reactor designs are typically limited by heat transfer, rather than by reaction kinetics. Consequently, the reactors are designed to promote heat exchange and tend to be large and heavy.

Partial oxidation reformers react the fuel with a sub-stoichiometric amount of oxygen. The initial oxidation reaction results in heat generation and high temperatures. The heat generated from the oxidation reaction raises the gas temperature, and by injecting an appropriate amount of steam into this gas mixture, steam reforming reaction can take place. The oxidation step may be conducted with or without a catalyst.

2. LITERATURE SURVEY

2.1. Fuel Cells

2.1.1. Fuel Cell Operation

Fuel cells are electrochemical devices which convert the chemical energy stored in a fuel into electrical energy, with heat as a by-product. Higher efficiencies and significantly lower emissions than conventional technologies in addition to their quiet operation and modular construction make fuel cells attractive for a wide range of applications like combined heat and power (CHP), distributed power generation and transport.

A fuel cell is comprised of an anode, an ion conducting electrolyte in the center, and a cathode. Fuel is oxidized at the anode, liberating electrons which flow via an external circuit to the cathode. The circuit is completed by a flow of ions across the electrolyte that separates the fuel and oxidant streams.

Practical cells typically generate a voltage of around 0.5-0.9 volts and power outputs of a few tens or hundreds of watts. Cells are therefore assembled in modules known as stacks of varying sizes, depending on the amount of electricity required.

2.1.2. Types and Applications of Fuel Cells

Typically, fuel cells are categorized according to their electrolytes. The electrolyte may consist of a liquid solution or a solid membrane material. There are basically five fuel cell versions.

Phosphoric acid fuel cells (PAFC) are suitable for stationary installation due to their large size and weight. They operate at moderate temperatures (453-473 K) and can use natural gas as fuel. These types of cells employ phosphoric acid electrolytes which are widely available.

The overall efficiency improves above the 40–50% range if the installations are used as cogeneration plants, and the waste heat is used to make hot water and/or steam. The advantage of PAFCs is that they are tolerant of reformate impurities. But they require the use of expensive platinum as catalyst. Power output is as much as 200kW. (Merewether, 2003).

Alkaline fuel cells (AFC) were first developed for spaceflight applications. These types of cells employ alkaline solution (potassium hydroxide in water) as the electrolyte. They operate at moderate temperatures (333-393 K) and do not require noble metal catalysts. But they are highly sensitive to CO_2 impurities and require pure hydrogen and oxygen as the fuel supply which make them unsuitable for mobile applications.

Molten carbonate fuel cells (MCFC) are suitable for stationary applications, power stations and industrial uses. They employ a molten carbonate salt as the electrolyte and operate at high temperatures (903-973 K). The high operating temperatures enables high efficiency and flexibility to use different types of fuels and inexpensive catalysts. They can produce power as much as 2 MW. Their main disadvantage is the corrosion enhanced by high operating temperature.

Solid oxide fuel cells (SOFC) are suitable for stationary applications, power stations and industrial uses. They use a solid metal oxide as the electrolyte and operate at high temperatures (1073-1273 K). They can produce power up to 100kW (Merewether, 2003).

PEM fuel cells are suitable for mobile applications due to their high power densities, compact dimensions, low weights, fast dynamic response and modular structures. They use a solid, polymer film as the electrolyte. They operate at moderate temperatures (333-363 K) and require pure hydrogen as the fuel. In addition to the vehicular applications, PEM fuel cells find application areas in small- scale CHP facilities and portable devices. Their main disadvantage is the low tolerance against impurities like sulphur and carbon monoxide.

2.2. Driving PEM Fuel Cells

Automobile manufacturers have decided that, given the state of the technology, the PEMFC has the best potential to replace the internal combustion engine for propulsion power due to the previously mentioned advantages including ability to fit (size and weight) the power plant under the hood of the car, the ability to start up quickly, the ability to meet the changing power demands (dynamic response) typical in a driving cycle, and cost. With the exception of cost, the PEFC would meet these requirements today if it could operate on hydrogen (Ahmed and Krumpelt, 2001).

2.2.1. On-board Storage

Hydrogen storage has been the subject of intensive research for many years. Hydrogen contains more chemical energy per weight than any hydrocarbon fuel, but it is also the lightest existing substance and therefore problematic to store effectively in small containers (Pettersson and Hjortsberg, 1999).

Vessels can be fuelled with hydrogen as a cryogenic liquid, low temperature compressed gas or ambient temperature compressed gas. Another method, which has been rigorously studied, involves the use of metals and alloys where the solids are reacted with hydrogen to form metal hydrides (Pettersson and Hjortsberg, 1999). As another method, compact, lightweight carbon adsorbent materials have become potential candidates for use in a hydrogen storage system. Of particular interest are the "engineered" nanostructured carbons such as carbon single-wall and multi-wall nanotubes and graphitic nanoparticles or cages (Dillon *et al*., 2003)

But these hydrogen storage technologies are expensive and combined with the low-energy density (implying a shorter driving range) (Ahmed and Krumpelt, 2001), and safety concerns, far from satisfying ideal vehicular performance.

2.2.2. On-board Fuel Conversion

An alternative is to convert hydrocarbon fuels to a hydrogen-rich gas (reformate) via an on-board fuel processor.

Conversion of hydrocarbon fuels to hydrogen can be carried out by several processes such as thermal cracking, steam reforming, carbon dioxide reforming, partial oxidation and autothermal reforming (Avcı, 2003)

$$CH_4 = C + 2H_2 \qquad \Delta H^0_{298} = 74.8 \text{ kJ mol}^{-1} \tag{2.1}$$

Direct decomposition of methane described in reaction (2.1) has several penalties in terms of heat requirement and carbon formation. Although carbon monoxide is not produced, thermal cracking is not considered to be a promising way of conducting on-board conversion. (Avcı, 2003)

$$CH_4 + H_2O = CO + 3H_2 \qquad \Delta H^0_{298} = 206.2 \text{ kJ mol}^{-1} \tag{2.2}$$

Steam reforming (Reaction 2.2) run on Ni based catalysts is a well known and cheapest method for large scale hydrogen production. These reformers are well suited for long periods of steady-state operation and can deliver relatively high concentrations of hydrogen (70% on a dry basis).

The carbon monoxide can be removed from the reformate gas stream by the water-gas shift reaction (Reaction 2.3).

$$CO + H_2O = CO_2 + H_2 \qquad \Delta H^0_{298} = -41.2 \text{ kJ mol}^{-1} \tag{2.3}$$

However the primary steam reforming reaction is strongly endothermic and reactor designs are typically limited by heat transfer. Consequently, the reactors are designed to promote heat exchange and tend to be large and heavy. In addition, indirect heat transfer (across a wall) makes conventional steam reformers less attractive for the rapid start and dynamic response needed in automotive applications (Ahmed and Krumpelt, 2001).

Partial oxidation reformers react the fuel with a sub-stoichiometric amount of oxygen. The initial oxidation reaction results in heat generation and high temperatures:

$$CH_4 + 2O_2 = CO_2 + 2H_2O \qquad \Delta H^0_{298} = -802.3 \text{ kJ mol}^{-1} \tag{2.4}$$

The heat generated from the oxidation reaction raises the gas temperature to over 1000 ^{0}C, whereby it is relatively easy to steam-reform the remaining (usually methane and other pyrolysis products) or added hydrocarbons or oxygenates, by injecting an appropriate amount of steam into this gas mixture. The oxidation step may be conducted with or without a catalyst (Ahmed and Krumpelt, 2001).

Autothermal reforming combines the heat effects of the partial oxidation and steam reforming reactions by feeding the fuel, water, and air together into the reactor. This process is carried out in the presence of a catalyst, which controls the reaction pathways and thereby determines the relative extents of the oxidation and steam reforming reactions. The steam reforming reaction absorbs part of the heat generated by the oxidation reaction, limiting the maximum temperature in the reactor. The net result is a slightly exothermic process. But in order to achieve the desired conversion and product selectivity, an appropriate catalyst is essential (Ahmed and Krumpelt, 2001).

The lower-temperature process provides many benefits for automotive applications including less fuel consumption at startup to heat the reformer to its operating temperature, wider choice of reactor materials ad less insulation required which in turn enables compact size and weight.

For kinetic considerations, practical reformers usually operate at temperatures above 600^{0}C. Since carbon formation is not predicted at 600^{0}C and O=C = 2, the ATR reaction is more attractive wherever size and weight constraints are acute (as in automobiles).

2.3. Autothermal reforming

2.3.1. Fuels

A number of fuels such as LPG, natural gas, methanol and gasoline are considered for their conversion into hydrogen. Fuels which can be stored in liquid form attract special

interest since it is a highly desired feature for vehicular applications. Coke formation is another concern in the selection of the fuel.

Methanol has advantages in terms of low impurities and ability to be stored in liquid form at ambient conditions. However, availability problems, lack of a widespread distribution network, and most importantly, its high toxicity makes it less attractive for vehicular applications. (Avc1, 2003)

Gasoline is another fuel which can be stored in liquid form. In addition, it is a readily available fuel which has a widespread distribution network. However, it is a complex fuel and includes a number of aromatics, which may lead to coke formation easily at the reforming conditions. (Avc1, 2003)

LPG, which is a mixture of propane and n-butane, is also advantageous since it can be stored in liquid form. It is an available and cheap fuel.

Natural gas, where the main constituent is methane, accounts for almost half the world's feedstock for hydrogen. It is an available fuel. But, the main difficulty for use of natural gas is that the methane is a very stable molecule and considerable energy input is required to trigger its conversion.

It has been found that longer chain hydrocarbons are most reactive and only small amounts of catalyst are required to initiate oxidation at low temperatures and provide the heat needed for steam reforming. (Ma *et al*., 1996).

In addition to hydrocarbons, autothermal ammonia decomposition provides an especially effective way to supply H_2 for use in the proton exchange membrane (PEM) fuel cell systems. This technique combines endothermic heterogeneous NH_3 decomposition reaction (into H_2 and N_2 on a supported catalyst) with the exothermic homogenous oxidation of ammonia (into N_2 and water) in the gas phase (Raissi, 2002).

Autothermal ammonia reformation is accomplished over a wide range of reformer temperatures. Furthermore, no NOx or any other undesirable species such as unreacted

oxygen is detected in the reformer effluent over a wide range of operating conditions (Raissi, 2002). However, the main disadvantage of autothermal reforming of ammonia is that the effluent stream needs be cooled down to a temperature compatible with PEM fuel cell operation. In addition, the scrubbing of the residual NH_3 (at ppm levels) in the effluent stream may also be necessary. (Raissi, 2002, Ogden, 2001). Its extreme toxicity and adverse health effects is another major drawback for its use in vehicular applications.

2.3.2. Catalysts

Although all reactions can be promoted by one catalyst, it has been found that use of separate oxidation and steam reforming catalysts are more effective (Ma and Trimm 1996).

Ni-based catalysts offer an appreciable catalyst activity for steam reforming reaction, in addition to a good stability and low price. This type of catalysts available in commerce is composed of NiO supported on ceramic materials. (Freni *et al*., 2000).

The catalysts based on the use of noble metals seem to be more active, but they are 100–150 times more expensive. Among different noble metals, activity of various noble metals for methane steam reforming has been found out to be Ru =Rh > Ni > Ir > Pd = Pt >> Co = Fe. . (Freni *et al*., 2000).

It has been found that Ni is a less effective catalyst than Pt in promoting the oxidation of light hydrocarbons. (Ma *et al*., 1996).

Catalysts can be deposited on the same support (one bed system) or on different supports (two bed system). Previous studies for the autothermal reforming of light hydrocarbons revealed that a bi-functional catalyst Pt-Ni/δ-Al_2O_3 is the most efficient system for hydrogen production by both oxidation and steam reforming in comparison to either a dual bed of Pt/δ-Al_2O_3 and commercial Ni based catalyst (Ni-com), or a single bed of physically mixed Pt/δ- Al_2O_3 and Ni-com. (Ma and Trimm 1996).

2.3.3. Integrated Reactor Concepts

Many concepts have been conceived and realized industrially of how the endo- and exothermic reactions can be reasonably combined.

The three main concepts are simultaneous, asymmetric and symmetric operations. (Kolios *et al*., 2000)

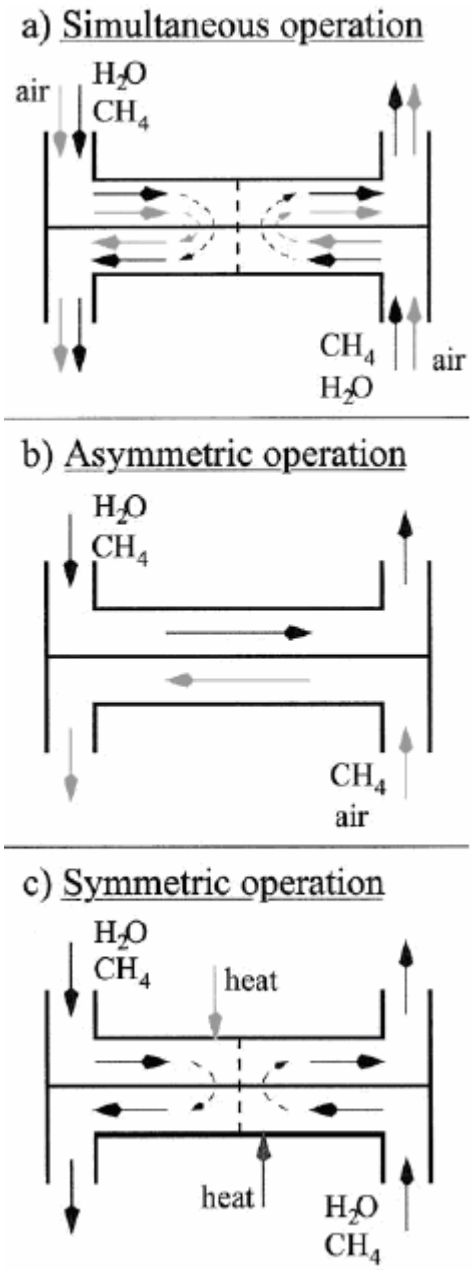

Figure 2.1 Simultaneous, symmetric and asymmetric operation for the coupling of exothermic and endothermic reactions (Kolios *et al*., 2000)

Under simultaneous operation the reactants for both (endo- and exothermic) reactions are mixed and all reactions run more or less in parallel. The rapid combustion results in a distinct temperature peak which is followed by the temperature decrease caused by the endothermic steam reforming. The length of the active catalyst zone and the residence time had to be properly adjusted to prevent excess temperatures, back reaction with decreasing temperatures or coke formation at temperatures below 750^0C (Kolios *et al*., 2000)

It has been shown (Hoang and Chan, 2004) that by this operation it is possible to convert, on a molar basis, 98% of the CH_4 supplied. For a cylindrical reformer shape where feed enters at one end and leaves at the other, the reformer temperature first increases along reformer length and reaches a peak within the front half of the reformer and then decreases a little in the rear half which indicates that the oxidation reaction dominates in the front half of the reformer, generating thermal energy for heating, while in the rear half, the endothermic steam reforming reactions take over and marginally cool down the reactor. The conversion behavior of the reformer strongly depends on A/F and W/F and to a lesser extent on the space velocity of the feed gas.

In order to better control the endo- and exothermic reaction zones, an alternative reformer configuration can be obtained by enclosing the cylindrical reformer mentioned above in a larger tube of low thermal conductivity. Catalyst is deposited on the inner and outer surfaces of the inner tube. This design offers the flexibility to deposit different catalysts on the inner and outer surfaces of the tube. The feed enters the inner tube, where the exothermic reaction takes place. A large fraction of the heat generated on the wall is transported across the tube wall towards the outer surface where the endothermic reactions take place. The hot effluents leaving thorough the annulus heat up the cold feed. It has been shown that the overall efficiency of the reformer strongly depends on the feed flow rate, furnace temperature and catalyst loading. (Ioannides and Verykios, 1998)

Under asymmetric conditions the feed for the endothermic reaction always comes from one side and the feed for the exothermic reaction comes from the opposite side. Fuel gas mixed with air for the combustion reaction and process gas for the endothermic

synthesis reaction are fed counter currently through separate adjacent channels of the reactor.

This operation enables heating of the cold feeds by the respective hot effluents on both sides of the countercurrent reactor. Thus, a high temperature region is developed in the middle of the reactor with a high degree of conversion for the endothermic reaction and minimum fuel consumption for the combustion (Frauhammer *et al*., 1999).

The internal heat exchange plays the most important role for the optimization of the process. Through inert reactor zones a decoupling of chemical conversion and local temperature is possible which is necessary for an optimization of the temperature and conversion profiles.

It has been shown (Frauhammer *et al*., 1999) for the methane reforming that increasing the fuel gas flow rate until the total conversion of the fuel gas is obtained, increases the peak temperature, which favors the steam reforming such that 100% conversion of process gas can be achieved. But at the exit it drops due to the reverse reaction to a value of 74 %. With further increase of the fuel gas flow, no adequate increase of the peak temperature is obtained, but the amount of reverse reaction increases. A measure to prevent the detrimental reverse reaction is to limit the length of the active catalyst where total conversion has been obtained.

Under symmetric conditions, the feed for the endothermic reaction comes from both sides as in simultaneous operation and the necessary heat of reaction from the exothermic reaction is supplied directly or indirectly in the middle of the reactor.

In the present work, autothermal reforming of methane, which seems to be one of the promising alternatives in the context of non-stationary hydrogen generation for PEMFC, is studied. A dual bed system is selected where a platinum based catalyst is considered as the best active metal for fuel combustion and a Ni based catalyst is the preferred choice for the steam reforming of the remaining hydrocarbon. The reformer is modeled as a hollow cylindrical tube enclosed in a bigger one and operating under simultaneous operation.

3. MATHEMATICAL MODEL

3.1. Problem Geometry

The model reactor consists of a hollow ceramic tube with its inside and outside surfaces coated with a metal catalyst film. The ceramic tube is enclosed in a larger ceramic tube of low thermal conductivity.

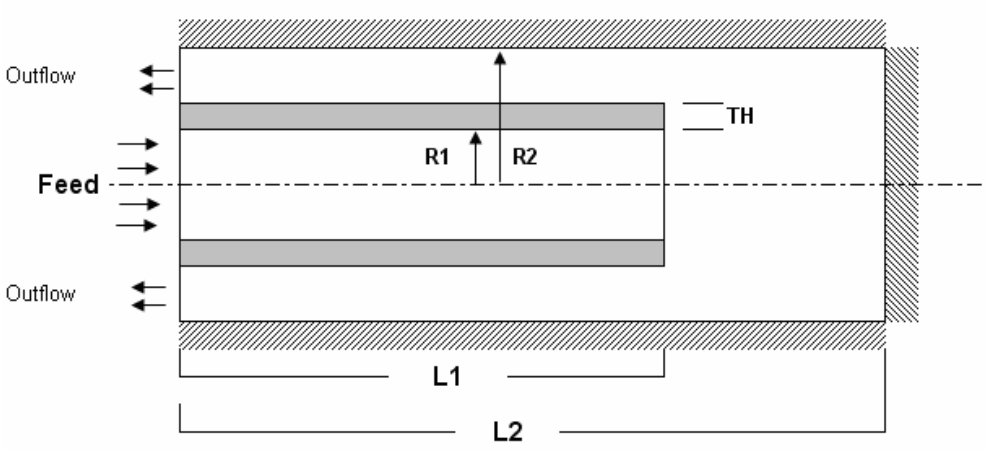

Figure 3.1 Geometry of Problem

3.2. Grid Structure

Non-uniform grid spacing is used in both directions with refined meshes near boundaries. In order to obtain a grid structure clustered near two wall surfaces, the following transformation (Andersen *et al*., 1984) is used:

$$\bar{y} = \alpha + (1-\alpha)\frac{\ln\left(\left\{\beta + \left[\frac{y(2\alpha+1)}{h}\right] - 2\alpha\right\} \Big/ \left\{\beta - \left[\frac{y(2\alpha+1)}{h}\right] + 2\alpha\right\}\right)}{\ln\left[\frac{\beta+1}{\beta-1}\right]} \qquad (3.1)$$

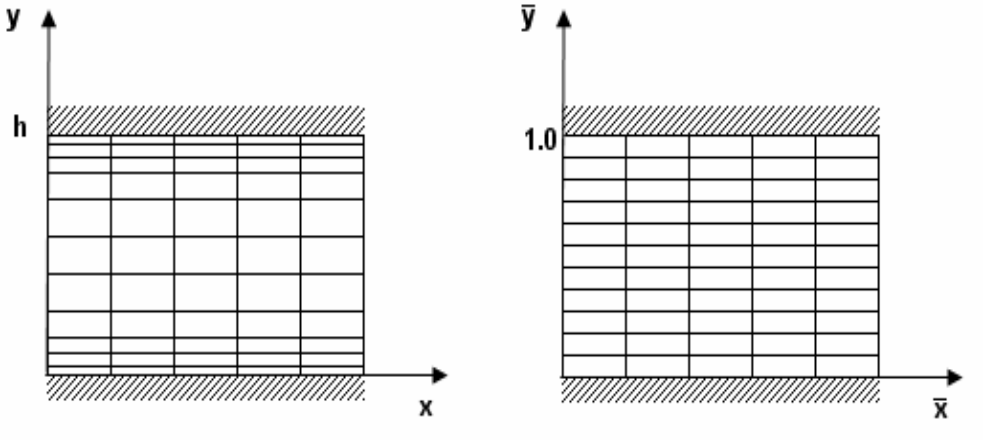

Figure 3.2 Clustered grids near walls

Inverse transformation with $\alpha = \frac{1}{2}$ gives clustered grids near $y = 0$ and $y = h$

$$y = h \frac{(\beta + 2\alpha)\left[\frac{(\beta+1)}{(\beta-1)}\right]^{\frac{\bar{y}-\alpha}{1-\alpha}} - \beta + 2\alpha}{(2\alpha+1)\left\{1+\left[\frac{(\beta+1)}{(\beta-1)}\right]^{\frac{\bar{y}-\alpha}{1-\alpha}}\right\}}$$

$$y = \frac{h}{2} \frac{(\beta+1)\left[\frac{(\beta+1)}{(\beta-1)}\right]^{2\bar{y}-1} - \beta + 1}{1+\left[\frac{(\beta+1)}{(\beta-1)}\right]^{2\bar{y}-1}}$$

If the number of cells between $0 < y < h$ is JN then for any j between $1 \le j \le JN$

$$\bar{y}_j = \frac{2j-1}{2\,JN}$$

$$y_j = \frac{h}{2}\frac{(\beta+1)\left[\frac{(\beta+1)}{(\beta-1)}\right]^{\left[\frac{2j-1}{JN}\right]-1} - \beta + 1}{1+\left[\frac{(\beta+1)}{(\beta-1)}\right]^{\left[\frac{2j-1}{JN}\right]-1}} \tag{3.2}$$

3.3. Species Mass Conservation

The rate of accumulation of species k within the volume will be equal to the sum of the net mass flux into the control volume and the net production rate of species k as a result of the chemical reactions.

$$\frac{\partial}{\partial t}\int_V \rho_k dV + \int_S \vec{\boldsymbol{m}}''_{\mathrm{k}} \cdot \vec{\boldsymbol{n}}\, dA = \int_V \dot{r}'''_k dV \tag{3.3}$$

Dividing by V and passing to the limit V→ 0, and for steady state conditions:

$$\vec{\nabla} \cdot \vec{\boldsymbol{m}}''_{\mathrm{k}} = \dot{r}'''_k \tag{3.4}$$

The total mass flux of species k will be the sum of the convective and diffusive mass fluxes. The convective flux of species k being $\rho_{\mathrm{k}}\vec{\boldsymbol{u}}$, and the diffusive flux $\vec{\boldsymbol{j}}_{\mathrm{k}}$ being equal to $\rho_{\mathrm{k}}\vec{\boldsymbol{v}}_{\mathrm{k}}$, the total mass flux $\vec{\boldsymbol{m}}''_{\mathrm{k}}$ of species k can be expressed as:

$$\vec{\boldsymbol{m}}''_{\mathrm{k}} = \rho_{\mathrm{k}}\vec{\boldsymbol{u}} + \rho_{\mathrm{k}}\vec{\boldsymbol{v}}_{\mathrm{k}} \tag{3.5}$$

If pressure and thermal diffusion are neglected, the diffusion velocity is related to the species gradients according to the mixture-averaged-formulation as follows (Kee et al., 1996):

$$\vec{\boldsymbol{v}}_{\boldsymbol{k}} = -D_{km}\frac{1}{X_k}\vec{\nabla}X_k$$

Replacing the molar fractions with mass fractions, diffusion velocity becomes:

$$\vec{v}_k = -\left[\frac{D_{km}}{Y_k \bar{M}}\right]\vec{\nabla}\left(Y_k \bar{M}\right) \tag{3.6}$$

Using Eq. (3.5) and (3.6) and also noting that $\rho_k = \rho Y_k$, Eq. (3.4) becomes

$$\vec{\nabla}\cdot\left(\rho\vec{u}Y_k\right) - \vec{\nabla}\cdot\left(\frac{\rho D_k}{\bar{M}}\ \vec{\nabla}\left(Y_k\bar{M}\right)\right) = \dot{r}_k'''$$

Assuming $Le_k = \dfrac{\lambda}{\rho D_{km} c_p}$ as constant and including the steady state continuity,

$$\left(\rho\vec{u}\ \right)\cdot\vec{\nabla}Y_k - \frac{1}{Le_k}\vec{\nabla}\cdot\left(\frac{\lambda}{c_p}\frac{1}{\bar{M}}\vec{\nabla}\left(Y_k\bar{M}\right)\right) = \dot{r}_k''' \tag{3.7}$$

Then the species mass conservation equation in 2-D axis symmetric polar coordinates for steady state neglecting pressure and thermal diffusion can be expressed as:

$$\frac{\partial^2 Y_k}{\partial z^2} + \frac{\partial^2 Y_k}{\partial r^2} + \left[c_1 - \frac{Le_k c_p}{\lambda}\rho u_z\right]\frac{\partial Y_k}{\partial z} + \left[c_2 - \frac{Le_k c_p}{\lambda}\rho u_r\right]\frac{\partial Y_k}{\partial r} + c_3 Y_k = -\frac{Le_k c_p}{\lambda}\dot{r}_k''' \tag{3.8}$$

where $\vec{\varsigma} = \vec{\nabla}\left(\ln\bar{M}\right)$ and $\vec{\phi} = \vec{\nabla}\left(\ln\left(\dfrac{\lambda}{c_p}\right)\right)$ being the auxiliary vectors;

$$c_1 = \varsigma_z + \phi_z$$

$$c_2 = \varsigma_r + \phi_r + \frac{1}{r}$$

$$c_3 = \varsigma_z\phi_z + \varsigma_r\phi_r + \frac{\partial\varsigma_r}{\partial r} + \frac{\partial\varsigma_z}{\partial z} + \frac{\varsigma_r}{r}$$

3.4. Energy Conservation

The most general form of energy conservation in temperature form (Shadid et al., 1996) can be expressed as

$$\rho c_p \frac{DT}{Dt} = -\vec{\nabla}\cdot\vec{q}'' + \frac{Dp}{Dt} + \psi + \dot{Q} + \sum_{k=1}^{KK}\vec{j}_k\cdot\vec{g}_k + \sum_{k=1}^{KK} h_k\vec{\nabla}\cdot\vec{j}_k - \sum_{k=1}^{KK} h_k r_k''' \tag{3.9}$$

The viscous dissipation term, ψ, and reversible change of mechanical energy into internal energy term (Dp/Dt) are dropped since they are small for low Mach number applications (Shadid et al., 1996). The body-force source term is omitted since the gravity vector is equal for all species k. Assuming no heat source or sink other than chemical reactions, the final form of the energy conservation equation in steady state becomes:

$$\rho c_p\left(\vec{u}\cdot\vec{\nabla}T\right) = -\vec{\nabla}\cdot\vec{q}'' + \sum_{k=1}^{KK} h_k\vec{\nabla}\cdot\vec{j}_k - \sum_{k=1}^{KK} h_k r_k''' \tag{3.10}$$

Neglecting the radiation, the diffusive heat flux can be expressed as:

$$\vec{q}'' = -\lambda\vec{\nabla}T + \sum_{k=1}^{KK} h_k\vec{j}_k \tag{3.11}$$

Then, using Eq. (3.6) and (3.11), Eq. (3.10) becomes

$$\vec{u}\cdot\vec{\nabla}T = \frac{1}{\rho c_p}\vec{\nabla}\left(\lambda\vec{\nabla}T\right) + \frac{1}{\rho c_p}\sum_{k=1}^{KK}\frac{1}{Le_k}\left(\frac{\lambda}{c_p}\right)\frac{1}{\bar{M}}\vec{\nabla}\left(Y_k\bar{M}\right)\cdot\vec{\nabla}h_k + \frac{1}{\rho c_p}\sum_{k=1}^{KK} h_k r_k''' \tag{3.12}$$

Then the energy conservation equation in 2-D axis symmetric polar coordinates for steady state neglecting the radiation can be expressed as:

$$\frac{\partial^2 T}{\partial r^2} + \frac{\partial^2 T}{\partial z^2} + \left[c_1 - \frac{\rho c_p u_r}{\lambda}\right]\frac{\partial T}{\partial r} + \left[c_2 - \frac{\rho c_p u_z}{\lambda}\right]\frac{\partial T}{\partial z} = S \tag{3.13}$$

where

$$c_1 = \frac{1}{r} + \frac{1}{\lambda}\frac{\partial \lambda}{\partial r}$$

$$c_2 = \frac{1}{\lambda}\frac{\partial \lambda}{\partial z}$$

$$S = -\sum_{k=1}^{KK} \frac{1}{Le_k}\frac{1}{c_p}\left[\frac{\partial Y_k}{\partial r}\frac{\partial h_k}{\partial r} + \frac{\partial Y_k}{\partial z}\frac{\partial h_k}{\partial z} + Y_k \varsigma_r \frac{\partial h_k}{\partial r} + Y_k \varsigma_z \frac{\partial h_k}{\partial z}\right] - \frac{1}{\lambda}\sum_{k=1}^{KK} h_k r_k'''$$

3.5. Boundary Conditions

3.5.1. Species Mass Conservation

Different boundary conditions, namely, inflow, outflow, symmetry, wall with no reaction and wall with reaction should be specified in the domain. All surfaces are assumed to be impermeable, and surface reactions take place only on the inner and outer surfaces of the separating internal wall.

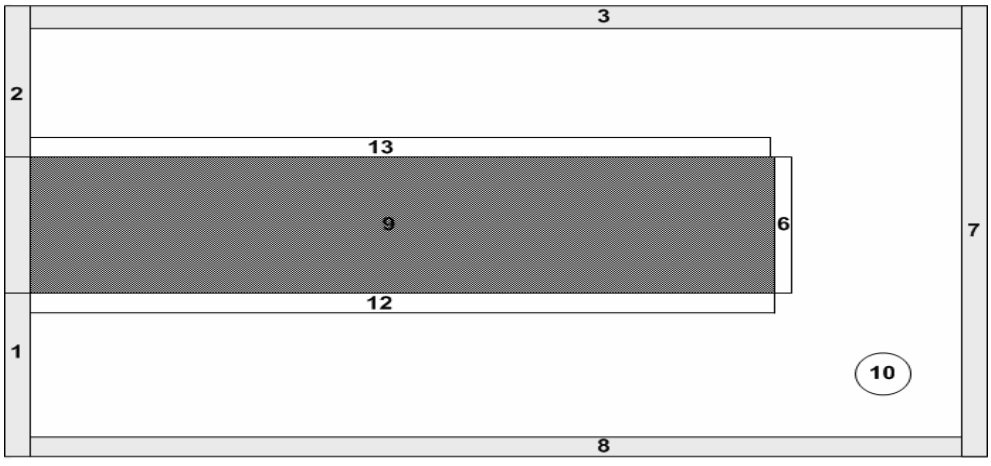

Figure 3.3 Different regions in the domain

A uniform mixture profile is specified at the inlet (region 1), while Zero-Neumann boundary conditions ($\vec{n} \cdot \vec{\nabla} Y_k = 0$) are valid for the outflow area (region 2) and the symmetry axis (region 8).

On boundaries corresponding to solid walls where no reactions are occurring (regions 7 and 3); the net flux of species is set to zero, $\vec{n}\cdot\left(\rho Y_k\vec{u}+\vec{j}_k\right)=0$. On boundaries corresponding to solid walls where surface reactions maybe occurring (regions 12 and 13), the flux of species k from the wall is equal to the net production rate of species k on the wall surface, $\vec{n}\cdot\left(\rho Y_k\vec{u}+\vec{j}_k\right)=r'''_{k,s}$, where $r'''_{k,s}$ is the net rate of production of species k per unit wall surface. With no slip condition for bulk velocity next to the walls, equations are reduced to diffusive flux only.

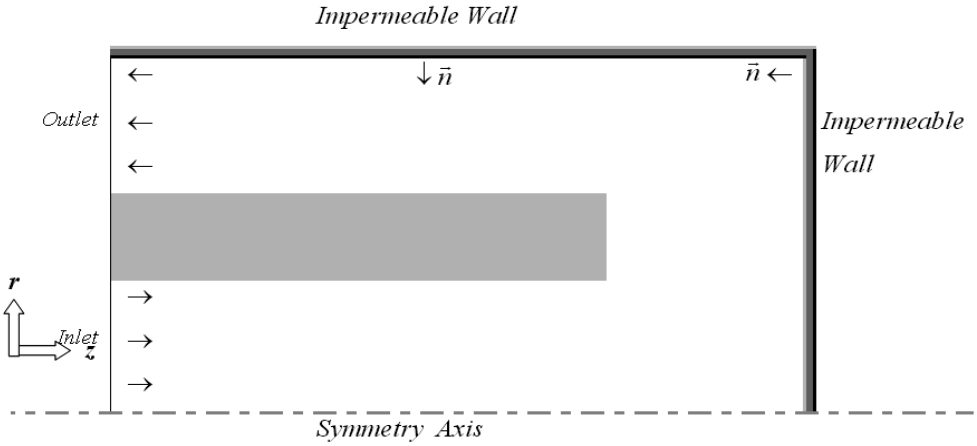

Figure 3.4 External Boundaries for the Species Conservation

Table 3.1 External Boundary Conditions for the Species Conservation

Region	**Type**	**Boundary Condition Specified**
Region 1	Inlet	$Y_k \quad given\left(k=1,2...KK\right)$
Region 2	Outlet	$\frac{\partial Y_k}{\partial z}=0 \quad \left(k=1,2...KK\right)$
Region 8	Symmetry Axis	$\frac{\partial Y_k}{\partial r}=0 \quad \left(k=1,2...KK\right)$
Region 7	Right Wall	$-\rho Y_k v_{k,z}=0$
Region 3	Top Wall	$\rho Y_k v_{k,r}=0$

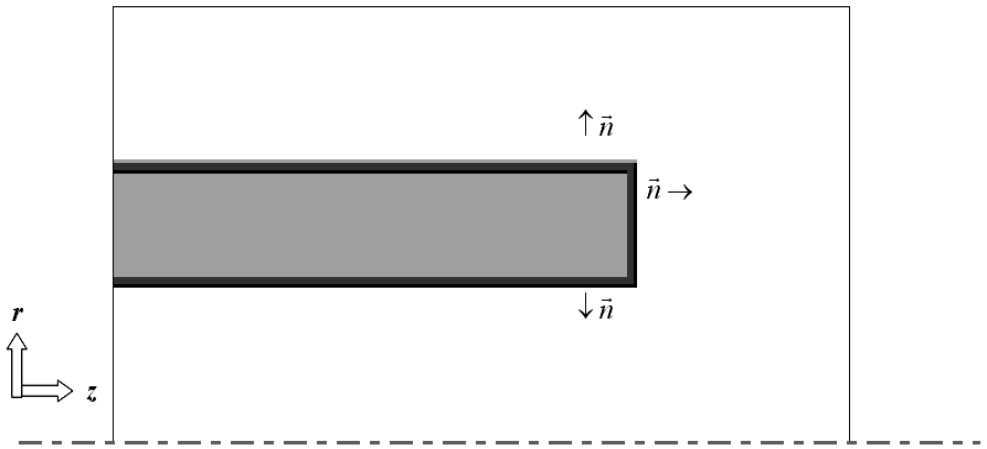

Figure 3.5 Internal Boundaries for the Species Conservation

Table 3.2 Internal Boundary Conditions for the Species Conservation

Region	**Type**	**Boundary Condition Specified**
Region 12	Separating Wall Inner Surface	$-\rho Y_k v_{k,r} = \dot{r}'''_{k,s}$
Region 13	Separating Wall Outer Surface	$\rho Y_k v_{k,r} = \dot{r}'''_{k,s}$
Region 6	Separating Wall Right Surface	$\rho Y_k v_{k,z} = 0$

3.5.2. Energy Conservation

A uniform temperature profile is specified at the inlet, while Zero-Neumann boundary conditions ($\vec{n} \cdot \vec{\nabla} T = 0$) are valid for outflow area and the symmetry axis. External walls, where no surface reaction takes place are assumed to be adiabatic ($\vec{q}'' = 0$), while for the internal separating walls where surface reactions may take place, an energy balance should be calculated.

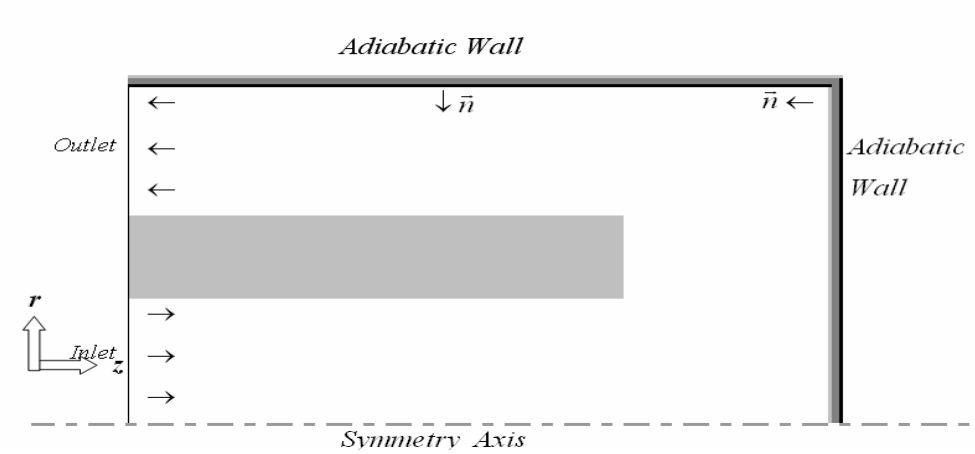

Figure 3.6 External Boundaries for the Energy Conservation

Table 3.3 External Boundary Conditions for the Energy Conservation

Region	**Type**	**Boundary Condition Specified**
Region 1	Inlet	$T \quad given$
Region 2	Outlet	$\frac{\partial T}{\partial z} = 0$
Region 8	Symmetry Axis	$\frac{\partial T}{\partial r} = 0$
Region 7	Right Wall	$\frac{\partial T}{\partial z} = 0$
Region 3	Top Wall	$\frac{\partial T}{\partial r} = 0$

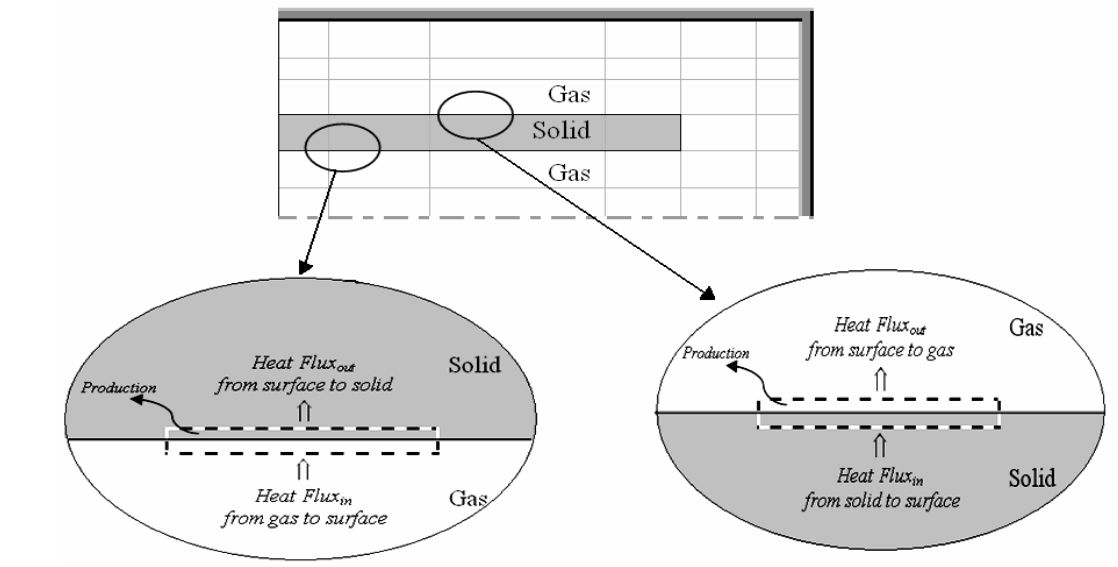

Figure 3.7 Internal Boundaries for the Species Conservation

On the inner surface of the separating wall, the heat flux from surface to solid will be the sum of the net heat flux from the gas to surface and the net production of heat on the surface as a result of chemical reactions. On the outer surface of the separating wall, the sum of the heat flux from solid and the net production of heat as a result of chemical reactions are transferred to gas. On the right surface, since no reaction will be occurring, the flux from the solid to the surface will be balanced by the flux from the surface to the gas.

Table 3.4 Internal Boundary Conditions for the Energy Conservation

Region	**Type**	**Boundary Condition Specified**
Region 12	Separating Wall Inner Surface	$\underbrace{-\lambda_g \frac{\partial T}{\partial r}\Big\|_{S^-} + \sum_{k=1}^{KK} \rho Y_k h_k v_{k,r}\Big\|_{S^-}}_{\text{Heat Flux in}} \underbrace{-\sum_{k=1}^{KK} h_k r'''_{k,s}\Big\|_{S}}_{\text{Heat Produced}} = \underbrace{-\lambda_s \frac{\partial T}{\partial r}\Big\|_{S^+}}_{\text{Heat Flux out}}$
Region 13	Separating Wall Outer Surface	$\underbrace{-\lambda_s \frac{\partial T}{\partial r}\Big\|_{S^-}}_{\text{Heat Flux in}} \underbrace{-\sum_{k=1}^{KK} h_k r'''_{k,s}\Big\|_{S}}_{\text{Heat Produced}} = \underbrace{-\lambda_g \frac{\partial T}{\partial r}\Big\|_{S^+} + \sum_{k=1}^{KK} \rho Y_k h_k v_{k,r}\Big\|_{S^+}}_{\text{Heat Flux out}}$
Region 6	Separating Wall Right Surface	$-\lambda_s \frac{\partial T}{\partial z}\Big\|_{S^-} = -\lambda_g \frac{\partial T}{\partial z}\Big\|_{S^+} + \sum_{k=1}^{KK} \rho Y_k h_k v_{k,z}\Big\|_{S^+}$

3.6. Calculation of Gas Phase Species Properties

3.6.1. Calculation of Pure Species Properties

7 different species are considered in the mixture. Table 3.5 shows molecular weights and assumed constant Lewis numbers.

Table 3.5 Species Considered

Compound	**Molecular Weight [kg/kmol]**	**Le**
CH_4	16.04	1.00
O_2	32.00	1.11
CO_2	44.01	1.39
H_2O	18.02	0.83
CO	28.01	1.00
H_2	2.02	1.00
N_2	28.01	1.00

The individual species thermal conductivities and heat capacities are calculated according to the following formulas where fitting coefficients obtained from Chemkin-II Transport Property Fitting Package are shown in Table 3.6 and 3.7 (Kee at al., 2003).

$$\lambda_k = a_k + b_k \ln T + c_k \left(\ln T\right)^2 + d_k \left(\ln T\right)^3 \tag{3.14}$$

$$c_{p,k} = a_k + b_k T + c_k T^2 + d_k T^3 + e_k T^4 \tag{3.15}$$

Table 3.6 Thermal Conductivity Coefficients

Compound	Thermal Conductivity [W/cm.K]			
	a	b	c	d
CH_4	-4.68E-01	1.08E+00	1.59E-01	-1.48E-02
O_2	-2.13E+00	2.99E+00	-2.87E-01	1.24E-02
CO_2	-1.40E+01	7.06E+00	-7.44E-01	2.89E-02
H_2O	1.63E+01	-5.89E+00	1.09E+00	-5.51E-02
CO	5.82E+00	-4.80E-01	2.11E-01	-1.14E-02
H_2	1.32E+01	-2.25E+00	3.81E-01	-1.57E-02
N_2	7.60E+00	-1.18E+00	3.03E-01	-1.54E-02

Table 3.7 Fitting Coefficients for the Heat Capacity Calculation

T	Compound	a	b	c	d	e
< 1000	CH_4	7.79E-01	1.75E-02	-2.78E-05	3.05E-08	-1.22E-11
< 1000	O_2	3.21E+00	1.13E-03	-5.76E-07	1.31E-09	-8.77E-13
< 1000	CO_2	2.28E+00	9.92E-03	-1.04E-05	6.87E-09	-2.12E-12
< 1000	H_2O	3.39E+00	3.47E-03	-6.35E-06	6.97E-09	-2.51E-12
< 1000	CO	3.26E+00	1.51E-03	-3.88E-06	5.58E-09	-2.47E-12
< 1000	H_2	3.30E+00	8.25E-04	-8.14E-07	-9.48E-11	4.13E-13
< 1000	N_2	3.30E+00	1.41E-03	-3.96E-06	5.64E-09	-2.44E-12
< 5000	CH_4	1.68E+00	1.02E-02	-3.88E-06	6.79E-10	-4.50E-14
< 5000	O_2	3.70E+00	6.14E-04	-1.26E-07	1.78E-11	-1.14E-15
< 5000	CO_2	4.45E+00	3.14E-03	-1.28E-06	2.39E-10	-1.67E-14
< 5000	H_2O	2.67E+00	3.06E-03	-8.73E-07	1.20E-10	-6.39E-15
<5000	CO	3.03E+00	1.44E-03	-5.63E-07	1.02E-10	-6.91E-15
< 5000	H_2	2.99E+00	7.00E-04	-5.63E-08	-9.23E-12	1.58E-15
< 5000	N_2	2.93E+00	1.49E-03	-5.68E-07	1.01E-10	-6.75E-15

3.6.2. Calculation of Mixture Averaged Properties

Mixture conductivity can be evaluated (Shadid et al., 1996) according to:

$$\lambda_{mix} = \frac{1}{2}\left(\sum_{k=1}^{KK} X_k \lambda_k + \frac{1}{\sum_{k=1}^{KK} \frac{X_k}{\lambda_k}} \right) \tag{3.16}$$

Mixture density is calculated from ideal gas law,

$$\rho = P\bar{M}\frac{1}{R}\frac{1}{T} \tag{3.17}$$

3.7. Chemical Kinetics

One step chemical kinetic models are employed for the reactions. Three different catalytic reactions are occurring on the surfaces of the separating internal wall.

3.7.1. Oxidation Reaction

According to the Langmuir-Hinshelwood model, reaction rate of methane oxidation (2.4) on Pt/δ-Al_2O_3 catalyst is given (Ma et al., 1996) in $\left[\frac{kmol}{kg.ca\ \ h}\right]$ as

$$R_1 = \frac{k_1 P_{CH_4} P_{O_2}^{1/2}}{\left(1 + K_{CH_4}^{C} P_{CH_4} + K_{O_2}^{C} P_{O_2}^{1/2}\right)^2} \times \eta_1 \tag{3.18}$$

Then the surface reaction rate can be expressed in $\left[\frac{mol}{cm^2\ s}\right]$ as

$$R_1 = \frac{k_1 P_{CH_4} P_{O_2}^{1/2}}{\left(1 + K_{CH_4}^{C} P_{CH_4} + K_{O_2}^{C} P_{O_2}^{1/2}\right)^2} \times \eta_1 \times \frac{cat\, w_1}{3600} \tag{3.19}$$

3.7.2. Steam Reforming Reaction

According to the model developed by Xu and Froment (1989) the rate of steam reforming reaction (2.2) can be expressed in $\left[\frac{kmol}{(kg.ca)\,h}\right]$ as

$$R_2 = \frac{k_2}{P_{H_2}^{2.5}} \left(P_{CH_4} P_{H_2O} - \frac{P_{H_2}^3 P_{CO}}{K_{e^2}} \right) x \frac{1}{Q_r^2} \times \eta_2 \tag{3.16}$$

where

$$Q_r = 1 + K_{CO} P_{CO} + K_{H_2} P_{H_2} + K_{CH_4} P_{CH_4} + \frac{K_{H_2O} P_{H_2O}}{P_{H_2}} \tag{3.17}$$

Then the surface reaction rate can be expressed in $\left[\frac{mol}{cm^2\, s}\right]$ as

$$R_2 = \frac{k_2}{P_{H_2}^{2.5}} \left(P_{CH_4} P_{H_2O} - \frac{P_{H_2}^3 P_{CO}}{K_{e^2}} \right) x \frac{1}{Q_r^2} \times \eta_2 \times \frac{cat\, w_2}{3600} \tag{3.22}$$

3.7.3. Water- Gas Shift Reaction

According to the model developed by Xu and Froment (1989) rate of water gas shift reaction (2.3) can be expressed in $\left[\frac{kmol}{(kg.ca)\,h}\right]$ as

$$R_3 = \frac{k_3}{P_{H_2}} \left(P_{CO} P_{H_2O} - \frac{P_{H_2} P_{CO_2}}{K_{e^3}} \right) x \frac{1}{Q_r^2} \times \eta_3 \tag{3.23}$$

where Q_r is again calculated according to Eq. (3.21)

Then the surface reaction rate can be expressed in $\left[\frac{mol}{cm^2\ s}\right]$ as

$$R_3 = \frac{k_3}{P_{H_2}}\left(P_{CO}P_{H_2O} - \frac{P_{H_2}P_{CO_2}}{K_{e^3}}\right) x \frac{1}{Q_r^2} \times \eta_3 \times \frac{cat\ w_3}{3600} \tag{3.24}$$

In all three rate equations, the kinetic rate constants k_j and adsorption coefficients K_k are calculated as (Hoang and Chan, 2004)

$$k_j = k_{oj} \times e^{\left(-E_j/RT\right)}$$

$$K_k = K_{0k} \times e^{(-\Delta H_k)/RT}$$

and the necessary kinetic parameters and constants are given in Table 3.8 through 3.11 (Hoang and Chan, 2004).

Table 3.8 Kinetic Parameters

Reaction		k_{0j} $kmol/kg.cat\ h$	E_j $kJ/kmol$
(2.4)	Oxidation	5.852 x 10^{17} bar $^{-15}$	204000
(2.2)	Steam Reforming	4.225 x 10^{15} bar $^{0.5}$	240000
(2.3)	Water-Gas Shift	1.955 x 10^{6} bar $^{-1}$	67130

Table 3.9 Equlibrium Constants

Reaction		K_{ej}
(2.2)	Steam Reforming	$5.75 \times 10^{12} \exp(-11476 / T)$
(2.3)	Water-Gas Shift	$1.26 \times 10^{-2} \exp(4639 / T)$

Table 3.10 Adsorption Coefficients

Species	K_{0k} $(/bar)$	H_k $kJ/kmol$
CH_4 (Combustion)	4.02×10^5	103500
O_2 (Combustion)	5.08×10^4 bar$^{0.5}$	66200
CH_4	6.65×10^{-4}	-38280
CO	8.23×10^{-5}	-70650
H_2	6.12×10^{-9}	-82900
H_2O	1.77×10^5 bar	88680

Considering the intraparticle mass transport limitations, the following effectiveness factors are suggested in the literature (Groote and Froment 1996).

Table 3.11 Effectiveness Factors for the Reaction Rates

Effectiveness Factor	**Reaction**	**Value**
η_1	Combustion	0.05
η_2	Steam Reforming	0.07
η_3	Water-Gas Shift	0.7

4. COMPUTER MODELING

4.1. Grid Generation

Using the input value of number of cells in the inner cylinder along the radial direction, the required numbers of cells along the separating wall and in the annulus are calculated in relation with the lengths. Then for each separate region with known number of cells together with lower and upper boundaries, r_j is calculated using the Eq. (3.2).

Table 4.1 Calculation of Radial Grids

Region	Grids	Formula
Inner Cylinder	$j = 1 \rightarrow \frac{1}{2}JJ$	$r_j = \frac{R1}{2}\frac{(\beta_r+1)\left[\frac{(\beta_r+1)}{(\beta_r-1)}\right]^{\left[\frac{2j-1}{JJ/2}\right]-1} - \beta_r + 1}{1+\left[\frac{(\beta_r+1)}{(\beta_r-1)}\right]^{\left[\frac{2j-1}{JJ/2}\right]-1}}$
Wall	$j = \frac{1}{2}JJ \rightarrow \frac{3}{4}JJ$	$r_j = R1 + \frac{TH}{2}\frac{(\beta_r+1)\left[\frac{(\beta_r+1)}{(\beta_r-1)}\right]^{\left[\frac{2(j-JIC)-1}{JW}\right]-1} - \beta_r + 1}{1+\left[\frac{(\beta_r+1)}{(\beta_r-1)}\right]^{\left[\frac{2(j-JIC)-1}{JW}\right]-1}}$
Annulus	$j = \frac{3}{4}JJ \rightarrow JJ$	$r_j = \frac{R1+TH+R2}{2}\frac{(\beta_r+1)\left[\frac{(\beta_r+1)}{(\beta_r-1)}\right]^{\left[\frac{2(j-JIC-JW)-1}{JOC}\right]-1} - \beta_r + 1}{1+\left[\frac{(\beta_r+1)}{(\beta_r-1)}\right]^{\left[\frac{2(j-JIC-JW)-1}{JOC}\right]-1}}$

In the axial direction, using the input value of number of cells and a given clustering location, z_i is calculated according to the below formula. Here, the grids are clustered at the end of separating wall.

Table 4.2 Calculation of Axial Grids

Region	Grids	Formula
Along the Wall	$i = 1 \rightarrow \frac{3}{4} II$	$z_i = \frac{L1}{2} \frac{(\beta_z+1)\left[(\beta_z+1)/(\beta_z-1)\right]^{\left[\frac{2i-1}{II/2}\right]-1} - \beta_z + 1}{1+\left[(\beta_z+1)/(\beta_z-1)\right]^{\left[\frac{2i-1}{II/2}\right]-1}}$
Rest	$i = \frac{3}{4} II \rightarrow II$	$z_i = L1 + \frac{LB}{2} \frac{(\beta_z+1)\left[(\beta_z+1)/(\beta_z-1)\right]^{\left[\frac{2(i-IIC)-1}{IOC}\right]-1} - \beta_z + 1}{1+\left[(\beta_z+1)/(\beta_z-1)\right]^{\left[\frac{2(i-IIC)-1}{IOC}\right]-1}}$

4.2. Discretization of Derivatives

Second order accurate discretizations are employed according to variably spaced grid configuration.

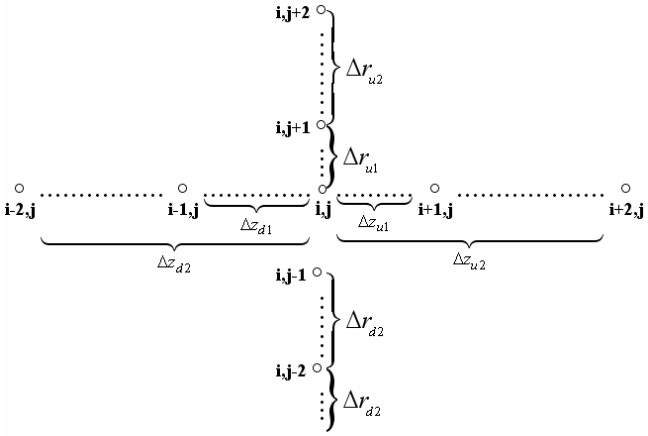

Figure 4.1 Grid Spacing

$$\Delta z_{um} = z_{i+m,j} - z_{ij} \quad ; \quad \Delta r_{um} = r_{i,j+m} - r_{ij}$$

$$\Delta z_{dm} = z_{ij} - z_{i-m,j} \quad ; \quad \Delta r_{dm} = r_{ij} - r_{i,j-m}$$

Forward or backward differences for boundaries, and central differences for interior grid points are used, while for convective terms, upwind difference is employed. In order to avoid repeating the same geometry dependent arithmetic operations for coefficients, they are calculated once and stored in arrays. The corresponding equation for each can be found in Table 4.3.

- First Order, Forward Differences

$$\left.\frac{\partial F}{\partial r}\right)_{ij} = -\left(frc_j\right)F_{ij} + \left(frn_j\right)F_{i,j+1} - \left(frnn_j\right)F_{i,j+2} + k\left(\Delta r\right)^2$$

$$\left.\frac{\partial F}{\partial z}\right)_{ij} = -\left(fzc_i\right)F_{ij} + \left(fze_i\right)F_{i+1,j} - \left(fzee_i\right)F_{i+2,j} + k\left(\Delta z\right)^2$$

- First Order, Backward Differences

$$\left.\frac{\partial F}{\partial r}\right)_{ij} = \left(brc_j\right)F_{ij} - \left(brs_j\right)F_{i,j-1} + \left(brss_j\right)F_{i,j-2} + k\left(\Delta r^2\right)$$

$$\left.\frac{\partial F}{\partial z}\right)_{ij} = \left(bzc_i\right)F_{ij} - \left(bzw_i\right)F_{i-1,j} + \left(bzww_i\right)F_{i-2,j} + k\left(\Delta z^2\right)$$

- First Order, Central Differences

$$\left.\frac{\partial F}{\partial r}\right)_{ij} = \left(crc_j\right)F_{i,j} + \left(crn_j\right)F_{i,j+1} - \left(crs_j\right)F_{i,j-1} + k\left(\Delta r^2\right)$$

$$\left.\frac{\partial F}{\partial z}\right)_{ij} = \left(czc_i\right)F_{i,j} + \left(cze_i\right)F_{i+1,j} - \left(czw_i\right)F_{i-1,j} + k\left(\Delta z^2\right)$$

- Second Order, Central Differences

$$\left.\frac{\partial^2 F}{\partial r^2}\right)_{ij} = -\left(crrc_j\right)F_{i,j} + \left(crrn_j\right)F_{i,j+1} + \left(crrs_j\right)F_{i,j-1} + k\left(\Delta r^2\right)$$

$$\left.\frac{\partial^2 F}{\partial z^2}\right)_{ij} = -\left(czzc_i\right)F_{i,j} + \left(czze_i\right)F_{i+1,j} + \left(czzw_i\right)F_{i-1,j} + k\left(\Delta z^2\right)$$

- Convective terms, Upwind Differences

$$\left.\frac{\partial F}{\partial r}\right)_{ij} = \left[F_{i,j-1} - F_{i,j}\right] \Big/ \left[r_j - r_{j-1}\right] \qquad u_r > 0$$

$$\left.\frac{\partial F}{\partial r}\right)_{ij} = \left[F_{i,j+1} - F_{i,j}\right] \Big/ \left[r_{j+1} - r_j\right] \qquad u_r < 0$$

$$\left.\frac{\partial F}{\partial z}\right)_{ij} = \left[F_{i-1,j} - F_{i,j}\right] \Big/ \left[z_i - z_{i-1}\right] \qquad u_z > 0$$

$$\left.\frac{\partial F}{\partial z}\right)_{ij} = \left[F_{i+1,j} - F_{i,j}\right] \Big/ \left[z_{i+1} - z_i\right] \qquad u_z < 0$$

Table 4.3 Coefficients in the Differencing Calculations

Differencing Method		
Forward	Backward	Central
$frc = \left[\frac{(\Delta r_{u1} + \Delta r_{u2})}{\Delta r_{u1} \Delta r_{u2}} \right]$	$brc = \left[\frac{(\Delta r_{d2} + \Delta r_{d1})}{\Delta r_{d1} \Delta r_{d2}} \right]$	$crc = \left[\frac{(\Delta r_{u1} - \Delta r_{d1})}{\Delta r_{u1} \Delta r_{d1}} \right]$
$frn = \left[\frac{\Delta r_{u2}}{\Delta r_{u1} (\Delta r_{u2} - \Delta r_{u1})} \right]$	$brs = \left[\frac{\Delta r_{d2}}{\Delta r_{d1} (\Delta r_{d2} - \Delta r_{d1})} \right]$	$crn = \left[\frac{\Delta r_{d1}}{\Delta r_{u1} (\Delta r_{u1} + \Delta r_{d1})} \right]$
$frnn = \left[\frac{\Delta r_{u1}}{\Delta r_{u2} (\Delta r_{u2} - \Delta r_{u1})} \right]$	$brss = \left[\frac{\Delta r_{d1}}{\Delta r_{2} (\Delta r_{d2} - \Delta r_{d1})} \right]$	$crs = \left[\frac{\Delta r_{u1}}{\Delta r_{d1} (\Delta r_{u1} + \Delta r_{d1})} \right]$
$fzc = \left[\frac{(\Delta z_{u1} + \Delta z_{u2})}{\Delta z_{u1} \Delta z_{u2}} \right]$	$bzc = \left[\frac{(\Delta z_{d2} + \Delta z_{d1})}{\Delta z_{d1} \Delta z_{d2}} \right]$	$crrc = \left[\frac{2}{\Delta r_{u1} \Delta r_{d1}} \right]$
$fze = \left[\frac{\Delta z_{u2}}{\Delta z_{u1} (\Delta z_{u2} - \Delta z_{u1})} \right]$	$bzw = \left[\frac{\Delta z_{d2}}{\Delta z_{d1} (\Delta z_{d2} - \Delta z_{d1})} \right]$	$crrn = \left[\frac{2}{\Delta r_{u1} (\Delta r_{u1} + \Delta r_{d1})} \right]$
$fzee = \left[\frac{\Delta z_{u1}}{\Delta z_{u2} (\Delta z_{u2} - \Delta z_{u1})} \right]$	$bzww = \left[\frac{\Delta z_{d1}}{\Delta z_{2} (\Delta z_{d2} - \Delta z_{d1})} \right]$	$crrs = \left[\frac{2}{\Delta r_{d1} (\Delta r_{u1} + \Delta r_{d1})} \right]$
		$czc = \left[\frac{(\Delta z_{u1} - \Delta z_{d1})}{\Delta z_{u1} \Delta z_{d1}} \right]$
		$cze = \left[\frac{\Delta z_{d1}}{\Delta z_{u1} (\Delta z_{u1} + \Delta z_{d1})} \right]$
		$czw = \left[\frac{\Delta z_{u1}}{\Delta z_{d1} (\Delta z_{u1} + \Delta z_{d1})} \right]$
		$czzc = \left[\frac{2}{\Delta z_{u1} \Delta z_{d1}} \right]$
		$czze = \left[\frac{2}{\Delta z_{u1} (\Delta z_{u1} + \Delta z_{d1})} \right]$
		$czzw = \left[\frac{2}{\Delta z_{d1} (\Delta z_{u1} + \Delta z_{d1})} \right]$

4.3. Discrete Form of Species Conservation Equation

The conservation equation, Eq. (3.8) derived before, is discretized according to the methods given above so that it obtained the following generic form:

$$a_{ij}Y_{i,j} + b_{ij}Y_{i+1,j} + c_{ij}Y_{i-1,j} + d_{ij}Y_{i,j+1} + e_{ij}Y_{i,j-1} + f_{ij}Y_{i+2,j} + g_{ij}Y_{i-2,j} + h_{ij}Y_{i,j+2} + l_{ij}Y_{i,j-2} = S_{ij}$$

Table 4.4 Discrete Form of the Species Conservation Equation with respect to Regions

Region	Discrete Form
1 and 9	$a_{ij}Y_{i,j} = S_{ij}$
2 and 6	$a_{ij}Y_{i,j} + b_{ij}Y_{i+1,j} + f_{ij}Y_{i+2,j} = S_{ij}$
3 and 12	$a_{ij}Y_{i,j} + e_{ij}Y_{i,j-1} + l_{ij}Y_{i,j-2} = S_{ij}$
7	$a_{ij}Y_{i,j} + c_{ij}Y_{i-1,j} + g_{ij}Y_{i-2,j} = S_{ij}$
8 and 13	$a_{ij}Y_{i,j} + d_{ij}Y_{i,j+1} + h_{ij}Y_{i,j+2} = S_{ij}$
10	$a_{ij}Y_{i,j} + b_{ij}Y_{i+1,j} + c_{ij}Y_{i-1,j} + d_{ij}Y_{i,j+1} + e_{ij}Y_{i,j-1} = S_{ij}$

4.3.1. Discrete Form of Energy Conservation Equation

The conservation equation, Eq. (3.13) derived before, is discretized according to the methods given above so that it obtained the following generic form:

$$a_{ij}T_{i,j} + b_{ij}T_{i+1,j} + c_{ij}T_{i-1,j} + d_{ij}T_{i,j+1} + e_{ij}T_{i,j-1} + f_{ij}T_{i+2,j} + g_{ij}T_{i-2,j} + h_{ij}T_{i,j+2} + l_{ij}T_{i,j-2} = S_{ij}$$

Table 4.5 Discrete Form of the Species Conservation Equation with respect to Regions

Region	Discrete Form
1	$a_{ij}T_{i,j} = S_{ij}$
2	$a_{ij}T_{i,j} + b_{ij}T_{i+1,j} + f_{ij}T_{i+2,j} = S_{ij}$
3	$a_{ij}T_{i,j} + e_{ij}T_{i,j-1} + l_{ij}T_{i,j-2} = S_{ij}$
6	$a_{ij}T_{i,j} + b_{ij}T_{i+1,j} + c_{ij}T_{i-1,j} + f_{ij}T_{i+2,j} + g_{ij}T_{i-2,j} = S_{ij}$
7	$a_{ij}Y_{i,j} + c_{ij}Y_{i-1,j} + g_{ij}Y_{i-2,j} = S_{ij}$
8	$a_{ij}Y_{i,j} + d_{ij}Y_{i,j+1} + h_{ij}Y_{i,j+2} = S_{ij}$
9 and 10	$a_{ij}T_{i,j} + b_{ij}T_{i+1,j} + c_{ij}T_{i-1,j} + d_{ij}T_{i,j+1} + e_{ij}T_{i,j-1} = S_{ij}$
12 and 13	$a_{ij}T_{i,j} + d_{ij}T_{i,j+1} + e_{ij}T_{i,j-1} + h_{ij}T_{i,j+2} + l_{ij}T_{i,j-2} = S_{ij}$

4.4. Algorithm

After an initial composition and temperature field guess for the domain, gas mixture properties, species mass fractions, reaction rates and temperature field are calculated. Using the updated T and Y fields, new mixture properties and reaction rates are computed, and this procedure is continued until a satisfactory convergence is met.

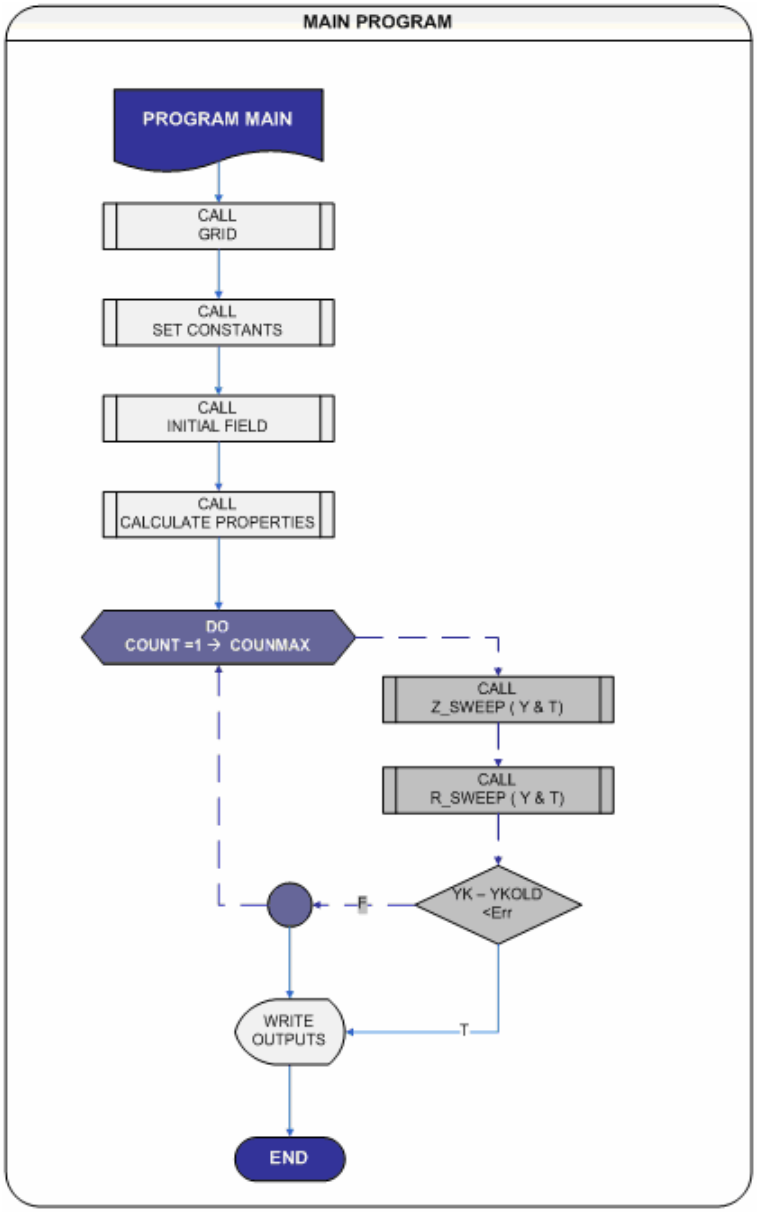

Figure 4.2 Main Program Flow

Gas properties, species mass concentration field, temperature field and reaction rates are swept in both directions. Species mass conservation and energy conservation equations are solved using Line-Gauss Siedel iteration.

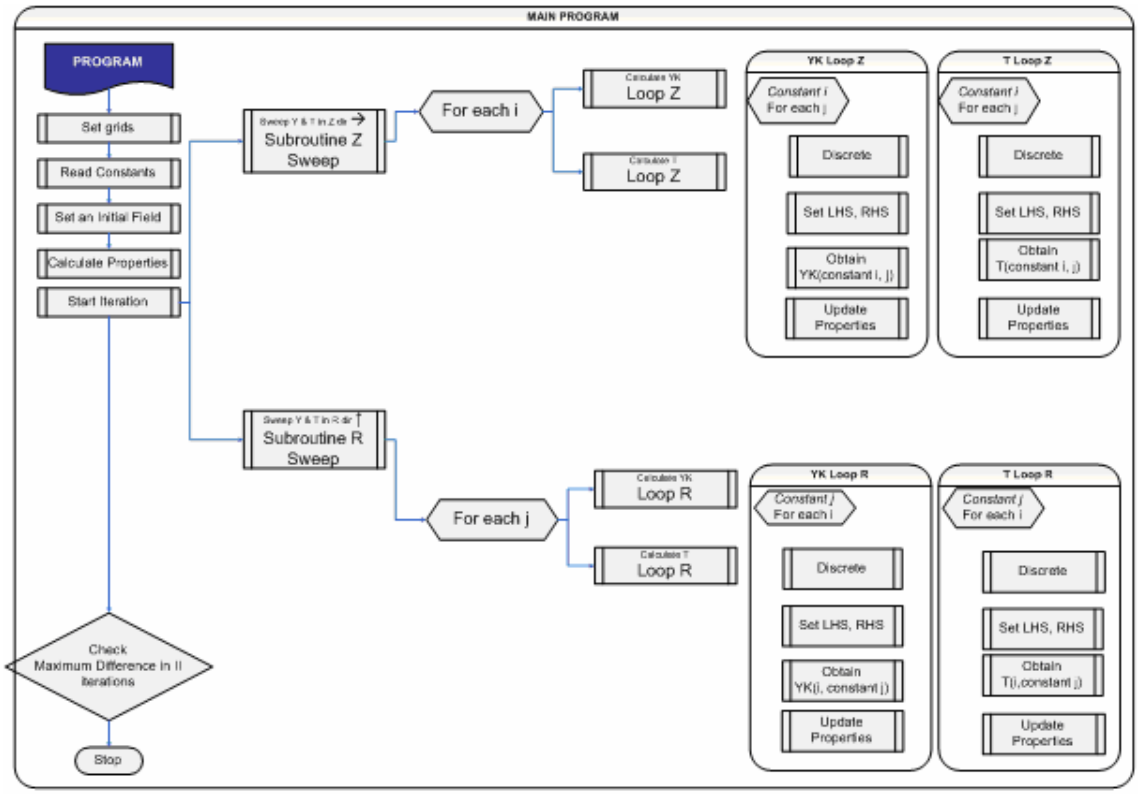

Figure 4.3 Detailed Program Flow

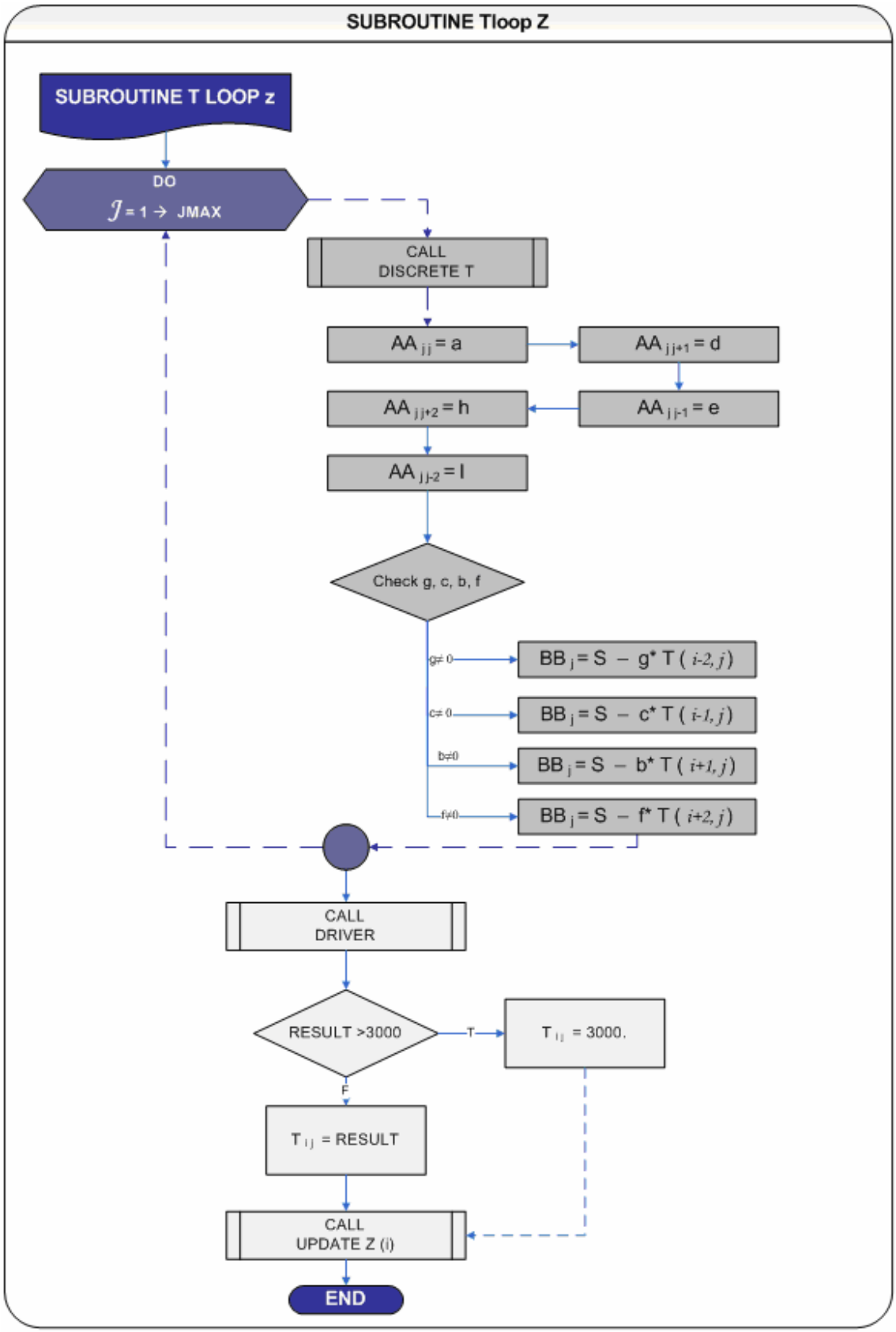

Figure 4.4 Flowchart for z- sweep of temperature field

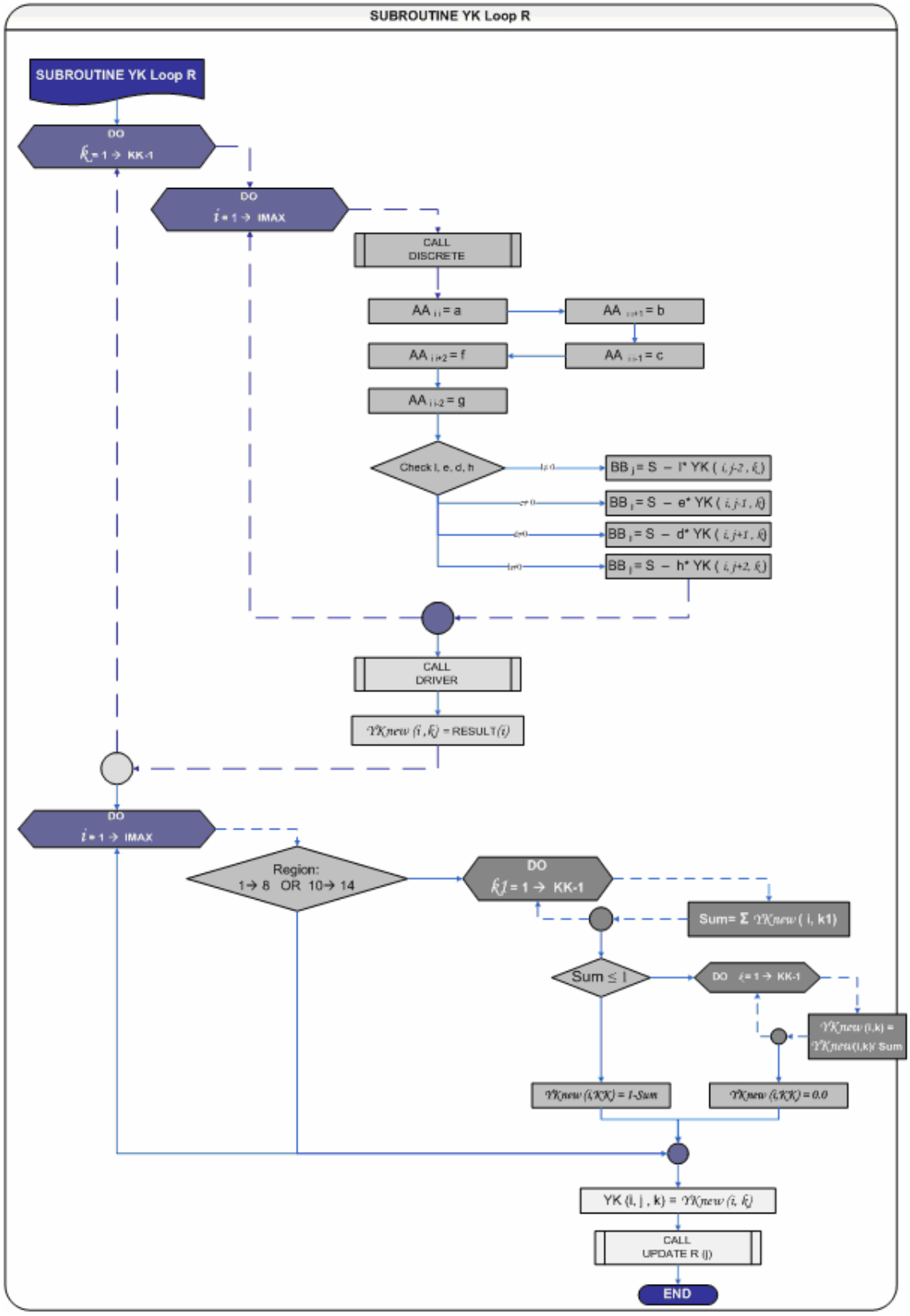

Figure 4.5 Flowchart for r- sweep of concentration field

5. RESULTS AND DISCUSSIONS

5.1. Simulation of Autothermal Hydrogen Production for Fuel Cells

An autothermal, dual catalyst, fixed bed reaction system under simultaneous operation for hydrogen production from methane is mathematically investigated.

A Pt/δ -Al_2O_3 catalyst is considered for oxidation reaction and a Ni/MgO- Al_2O_3 catalyst for the reforming reactions.

Effect of different feed ratios and the effect of catalyst deposition on the hydrogen output are analyzed.

5.2. Convergence History

Below data is presented as an example for the conditions of A/F : 3.5, W/F: 1.5, Catalyst deposition between 2.5—> 7.5 cm, feed flow rate of 30 cm3/s.

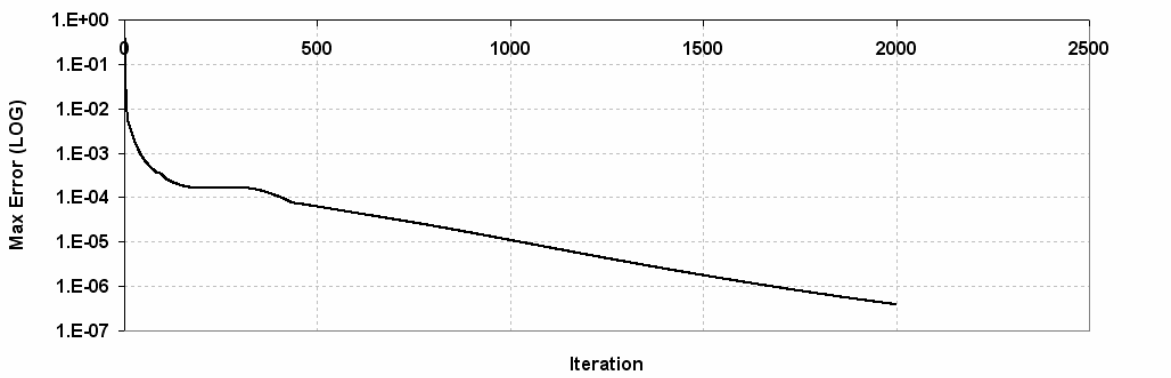

Figure 5.1 The observed maximum difference of the Y value of any species between two consecutive iterations

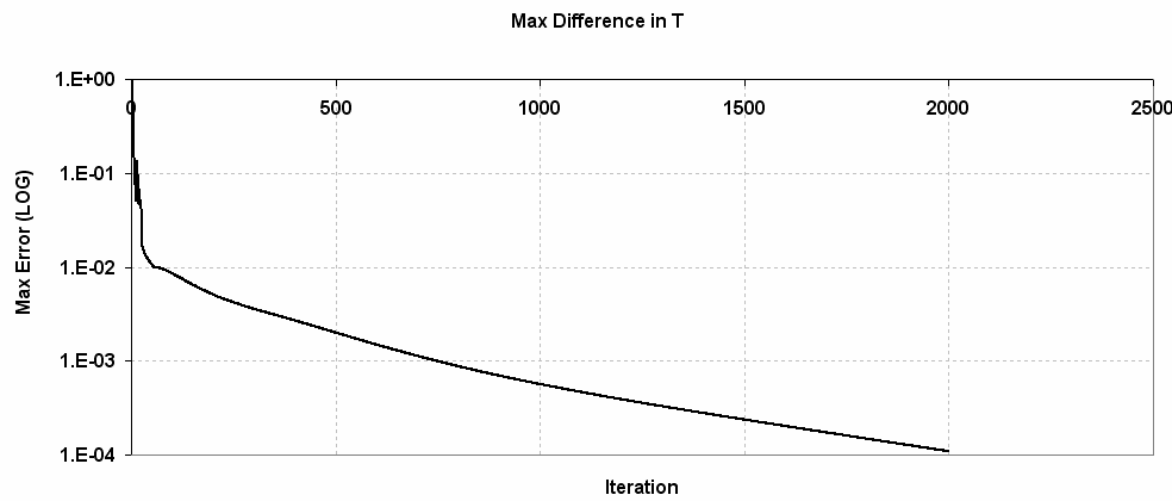

Figure 5.2 The observed maximum difference of the T values between two consecutive iterations

5.3. Temperature and Species Distributions

For the inlet conditions of A/F : 3.5, W/F: 1.5 the resultant species and temperature profiles are analyzed.

Both catalysts are deposited over the surface from 2.5 cm from the inlet to 7.5 cm. Figure 5.3 shows the geometry and positions of the catalysts.

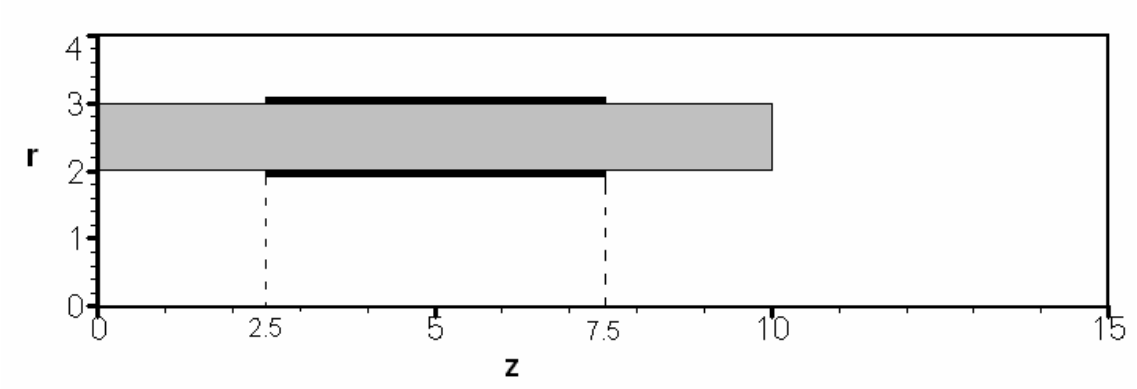

Figure 5.3 Reactor Geometry and Catalyst Deposition

Feed flow rate is 30 cm^3/s and resultant velocity field is shown in Figure 5.4.

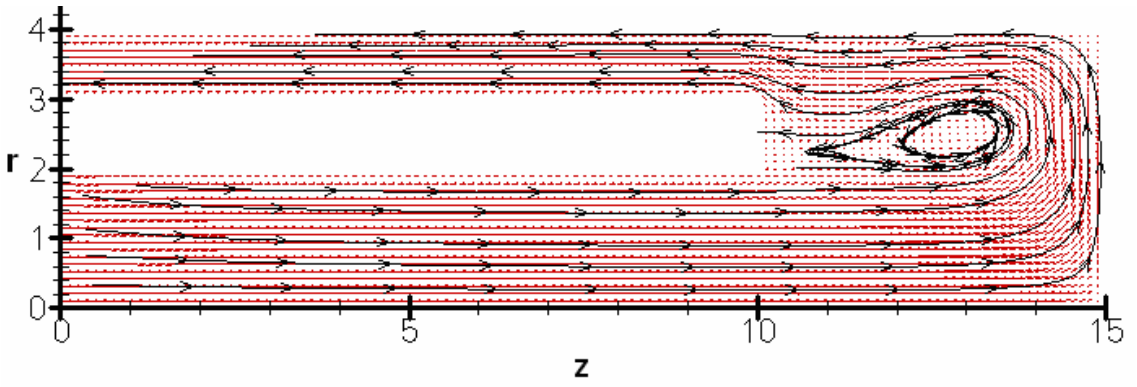

Figure 5.4 Velocity Field

Figure 5.5 through 5.10 show the contour plots of the mass concentrations of different species as a result of the given configuration. It can be seen that the relative concentration changes are directly related with the catalyst deposited area.

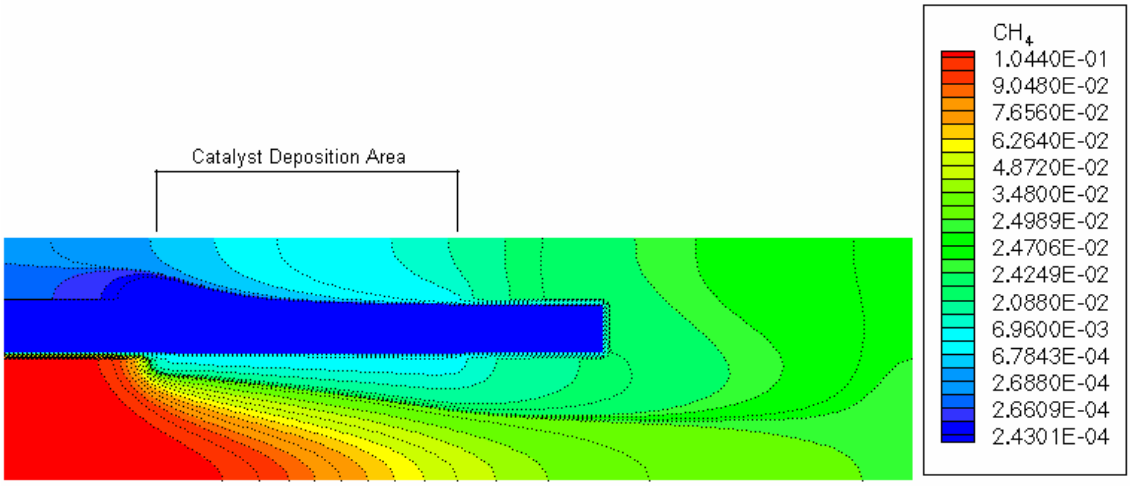

Figure 5.5 Methane Mass Fraction

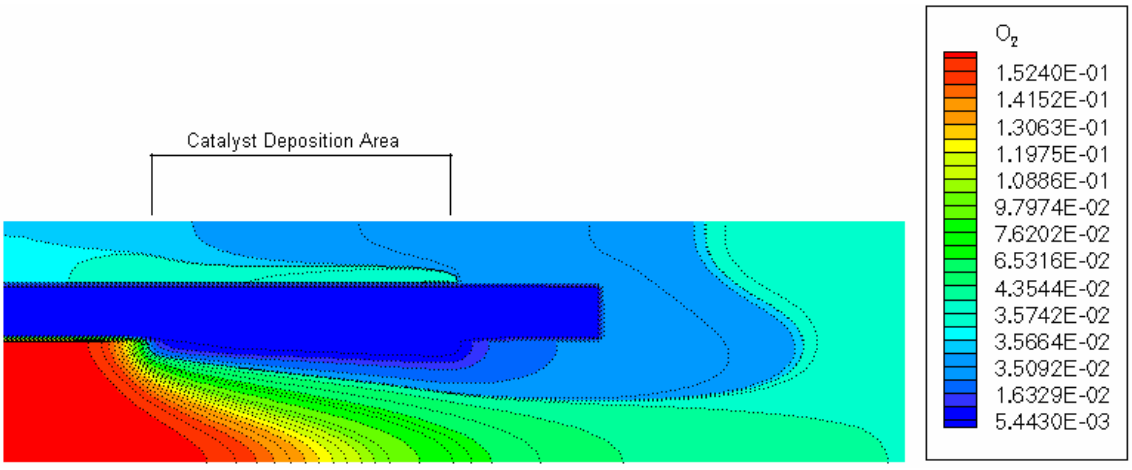

Figure 5.6 Oxygen Mass Fraction

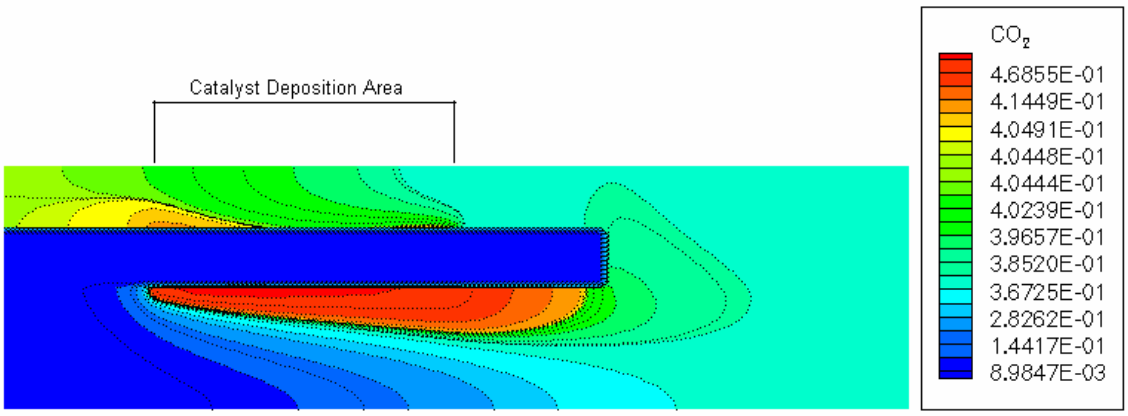

Figure 5.7 Carbon dioxide Mass Fraction

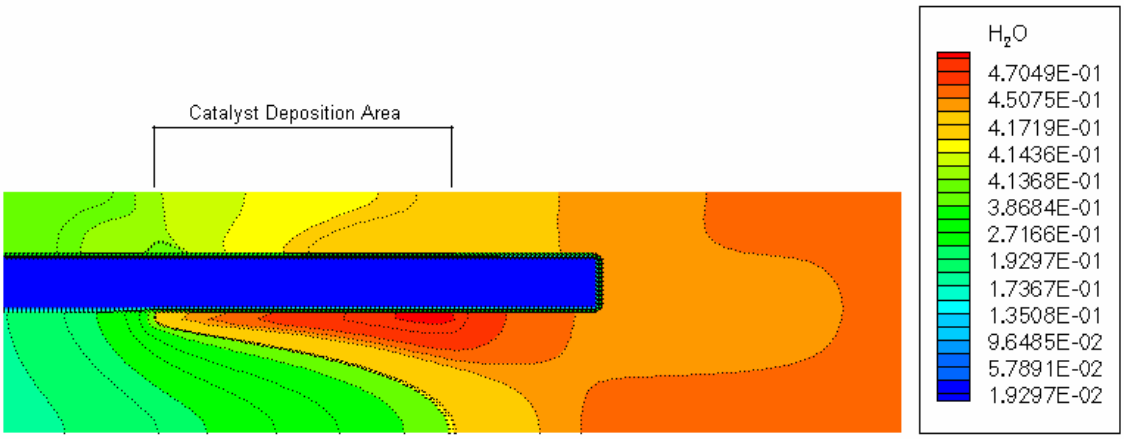

Figure 5.8 Water Mass Fraction

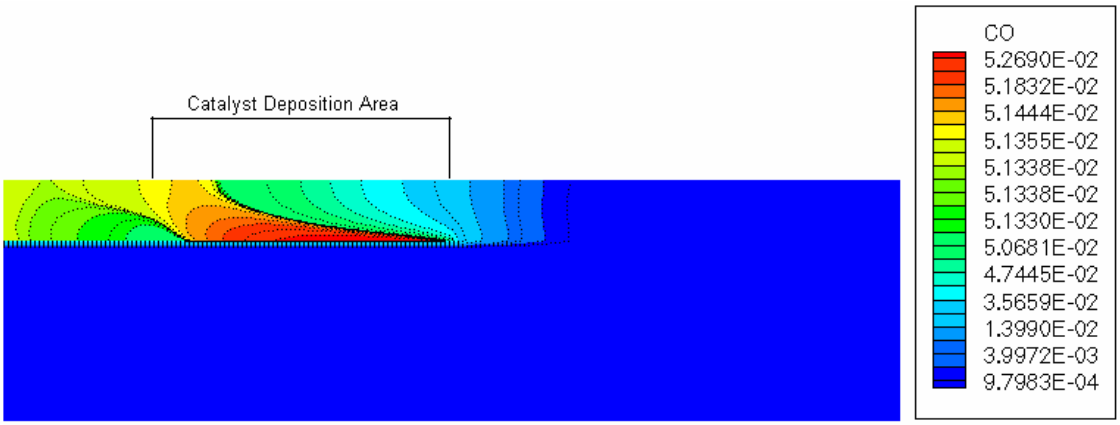

Figure 5.9 Carbon monoxide Mass Fraction

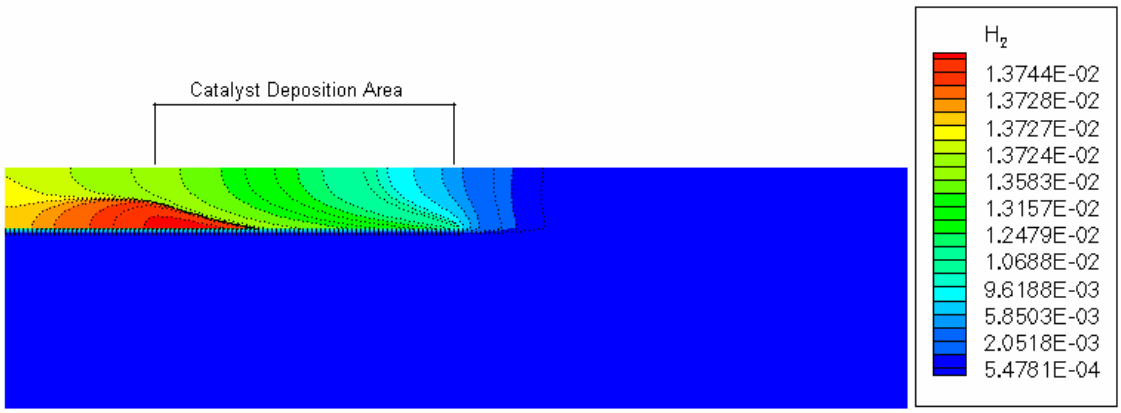

Figure 5.10 Hydrogen Mass Fraction

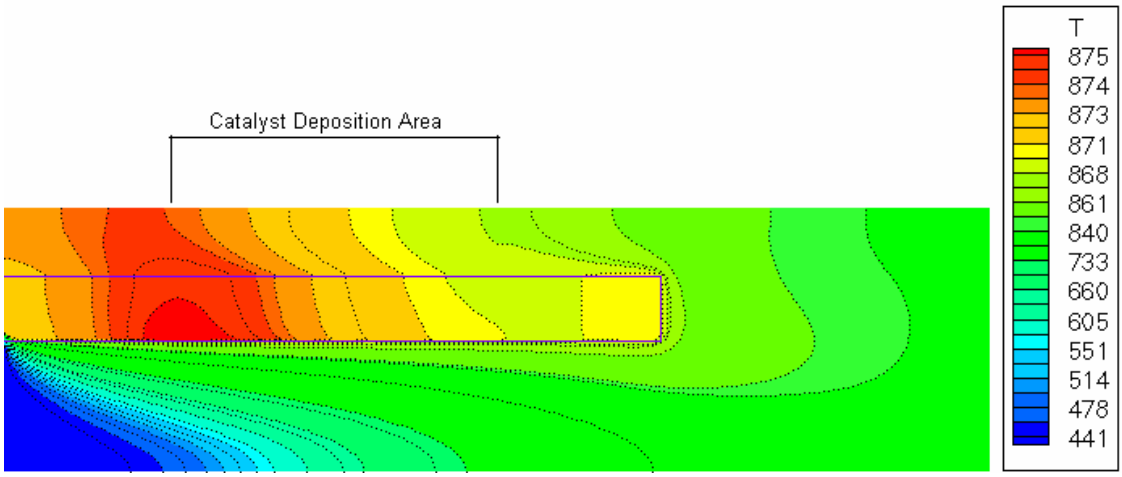

Figure 5.11 Temperature Field (K)

Figure 5.12 through Figure 5.14 shows the percentage of molar concentrations of the species at three different “r” positions of the reformer along the reformer length.

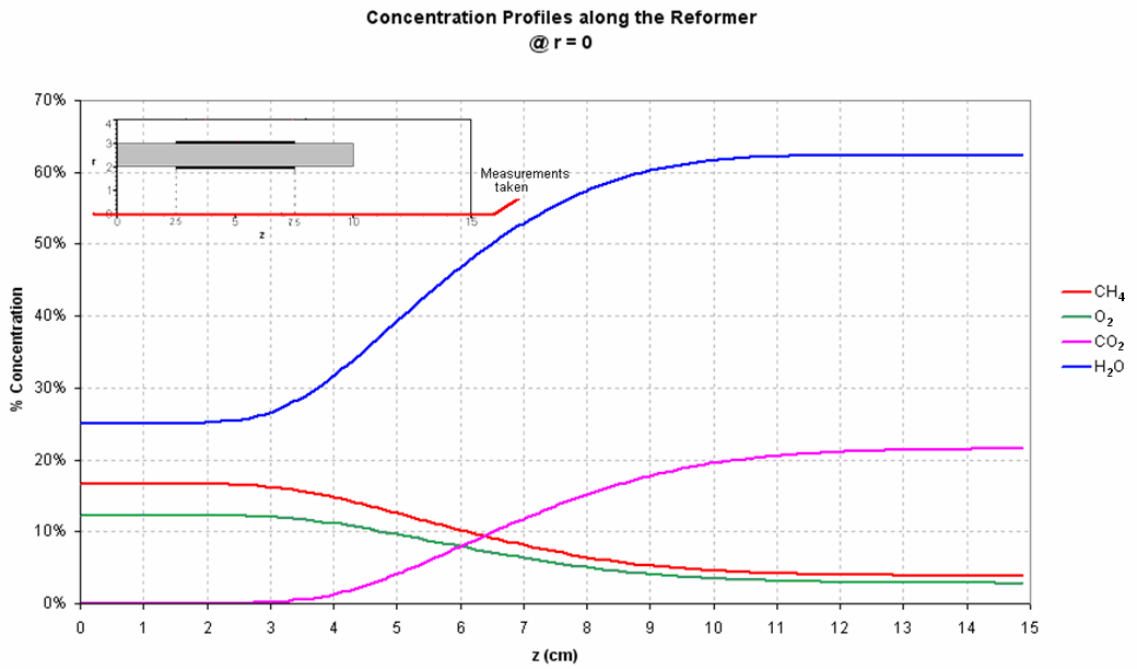

Figure 5.12 Concentration profiles at center along the reformer length

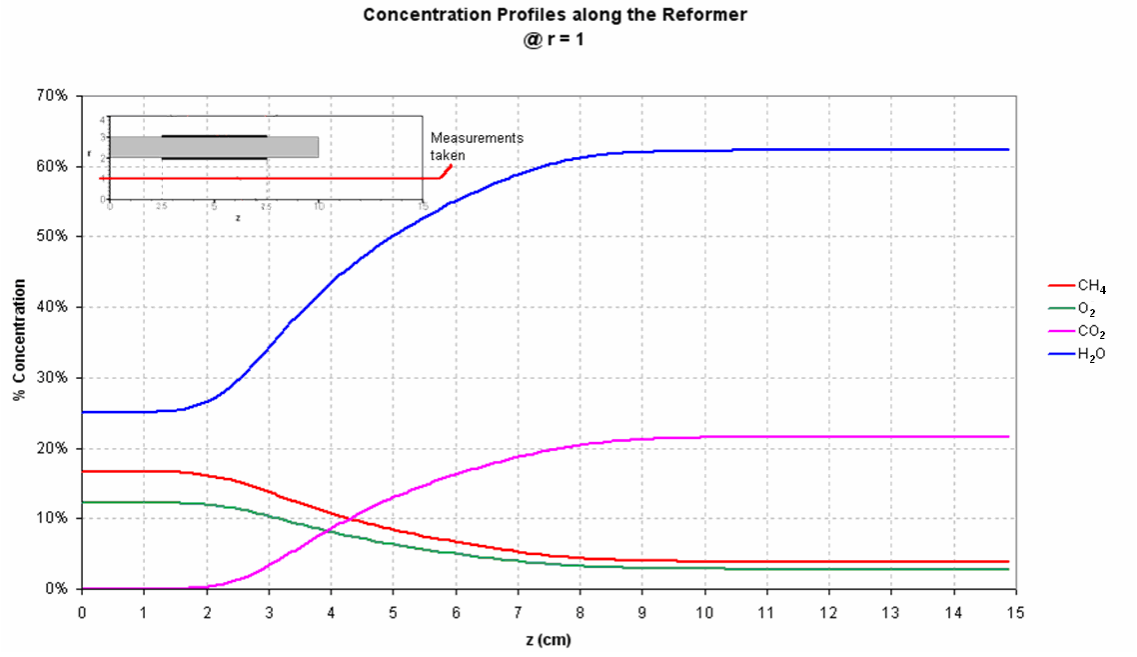

Figure 5.13 Concentration profiles at r = 1 cm (center for the inlet stream) along the reformer length

As can be seen, from Fig. 5.14 that the CO_2 and H_2O concentrations start to increase, while CH_4 and O_2 concentrations start to decrease after z = 2.5 cm, where the catalytic oxidation reaction starts to take place. The concentration of H_2O and CO_2 reaches their

maximum and CH_4 and O_2 to their minimum after catalytic reaction zone is passed, and stay approximately stable in the back part of the reformer.

Fig 5.15 shows the similar trend. The only difference is, since the measurements are taken at a position much closer to the reactive surface, concentration changes are much sensitive to the catalyst deposition area.

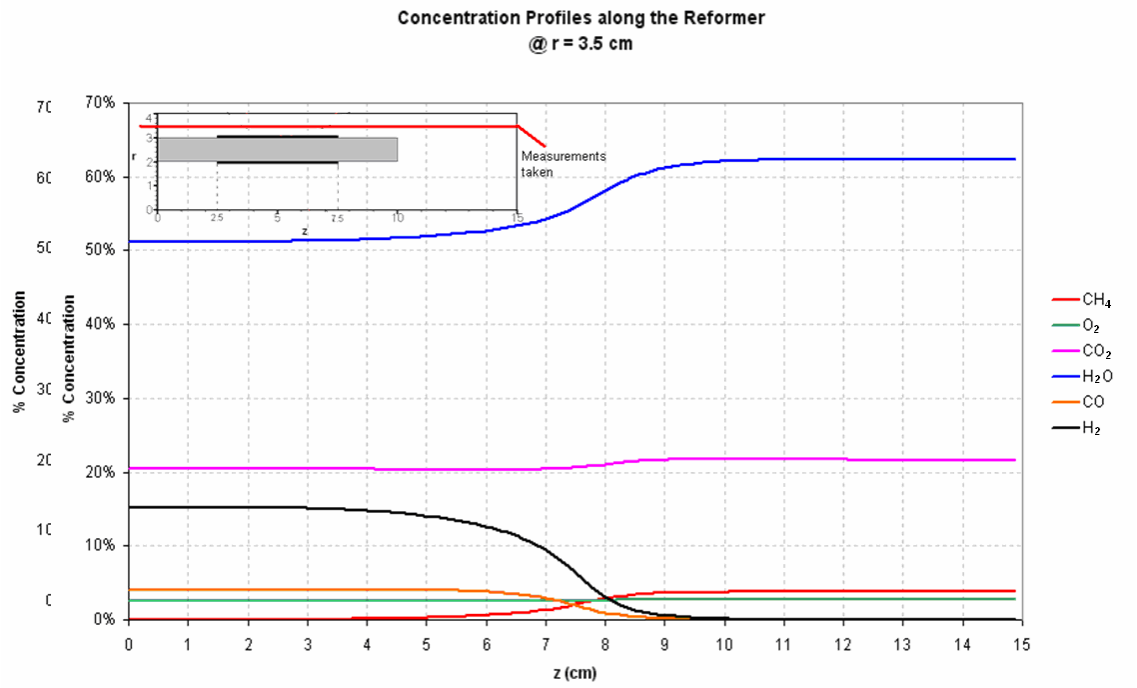

Figure 5.14 Concentration profiles at r = 3.5 cm (center for the outlet stream) along the reformer length

Fig. 5.16 shows the axial distribution of species at r = 3.5 cm, which is above the separating wall so that effects of steam reforming and water-gas shift reactions can be seen. Following the flow of gas, in the right most part of the graph the product gas concentrations after oxidation reaction is shown. Moving to the left, once z =7.5 cm is reached, the catalytic region starts which is accompanied with a rapid increase in H_2 and CO concentration while a decrease in H_2O and CH_4 concentrations. Concentrations reach a constant value towards the outlet (z= 0).

Fig. 5.17 shows the temperature variation along the reformer length. At the center, at r = 1 and at r = 2 cm, temperature rapidly increases due to exothermic oxidation reaction.

At r = 3 cm and above temperature values show small differences and almost constant. The product gases leave the reformer at 874 K.

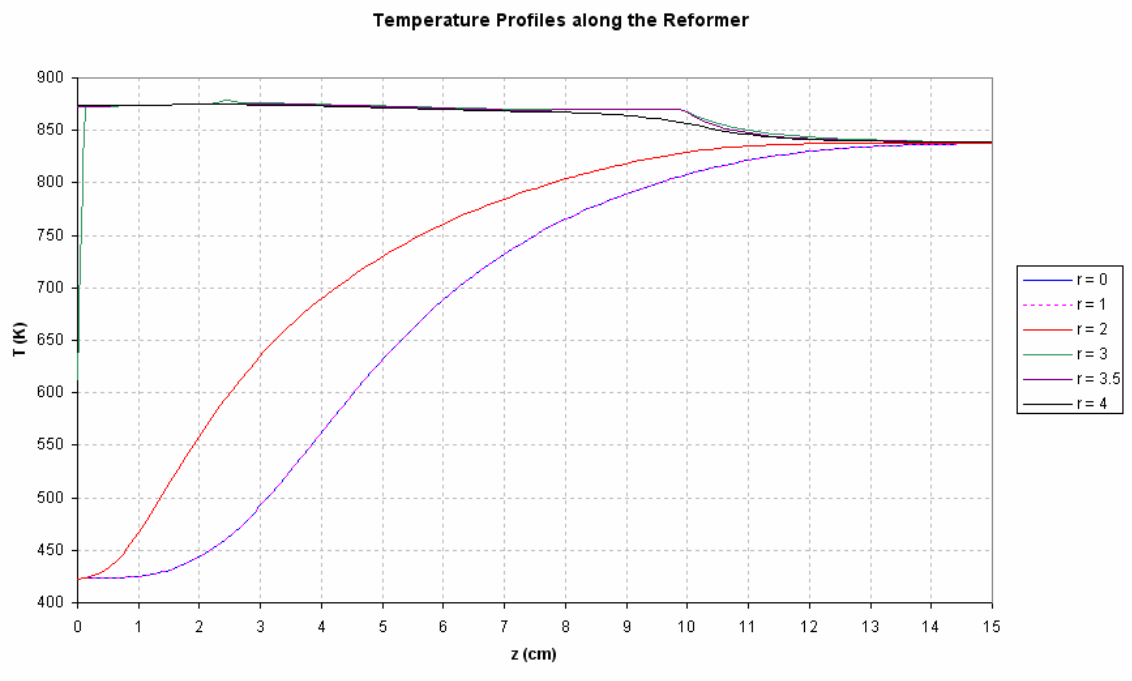

Figure 5.15 Temperature profiles at various locations along the reformer length

5.4. Effect of Feed Ratio

Effect of feed ratio on the product gas distribution is analyzed by changing only the molar air-to-fuel (A/F) and water-to-fuel (W/F) ratios while keeping the other parameters the same, namely, catalyst deposition according to Figure 5.5 and feed flow rate of 30 cm^3/s. Totally 35 different feed ratios are analyzed for A/F ratio varying between 2.0 and 4.0 and W/F ratio varying between 0.0 to 3.0. Inlet data is shown in Table 5.1.

Table 5.1 Different Feed Rations used for analysis

Feed Ratio	W/F	A/F		Feed Ratio	W/F	A/F
1	0.00	2.00		**21**	2.00	2.00
2	0.00	2.75		**22**	2.00	2.75
3	0.00	3.50		**23**	2.00	3.50
4	0.00	4.00		**24**	2.00	4.00
5	0.00	4.50		**25**	2.00	4.50
6	0.50	2.00		**26**	2.50	2.00
7	0.50	2.75		**27**	2.50	2.75
8	0.50	3.50		**28**	2.50	3.50
9	0.50	4.00		**29**	2.50	4.00
10	0.50	4.50		**30**	2.50	4.50
11	1.00	2.00		**31**	3.00	2.00
12	1.00	2.75		**32**	3.00	2.75
13	1.00	3.50		**33**	3.00	3.50
14	1.00	4.00		**34**	3.00	4.00
15	1.00	4.50		**35**	3.00	4.50
16	1.50	2.00				
17	1.50	2.75				
18	1.50	3.50				
19	1.50	4.00				
20	1.50	4.50				

Figure 5.16 shows the dry H_2 concentration in the product gas for different feed concentrations. In the figure, each spline represents the change of H_2 concentration with air-to-fuel ratio for a constant water-to-fuel ratio.

As can be seen, increasing the air-to-fuel ratio over a certain extent negatively affects the H_2 output for all W/F ratio selected since more of the fuel is being consumed in oxidation reactions.

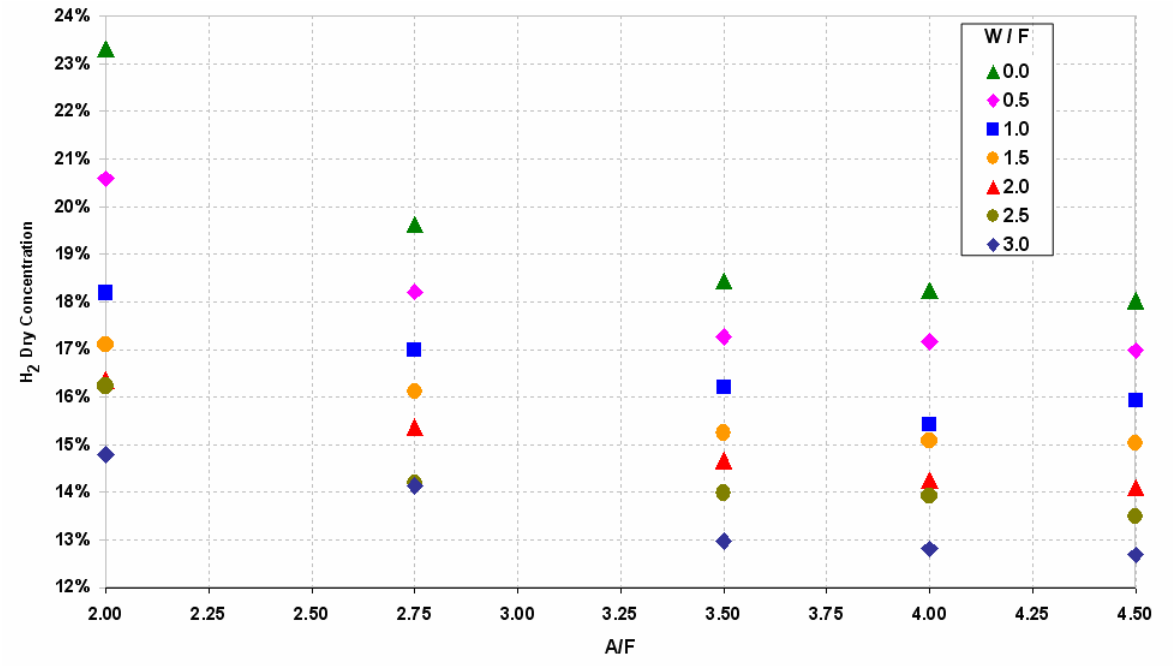

Figure 5.16 Change of H_2 (dry) output with feed ratio

Similarly, the dry CH_4 concentrations in the product gas can be seen in Figure 5.17, and CO in Figure 5.18.

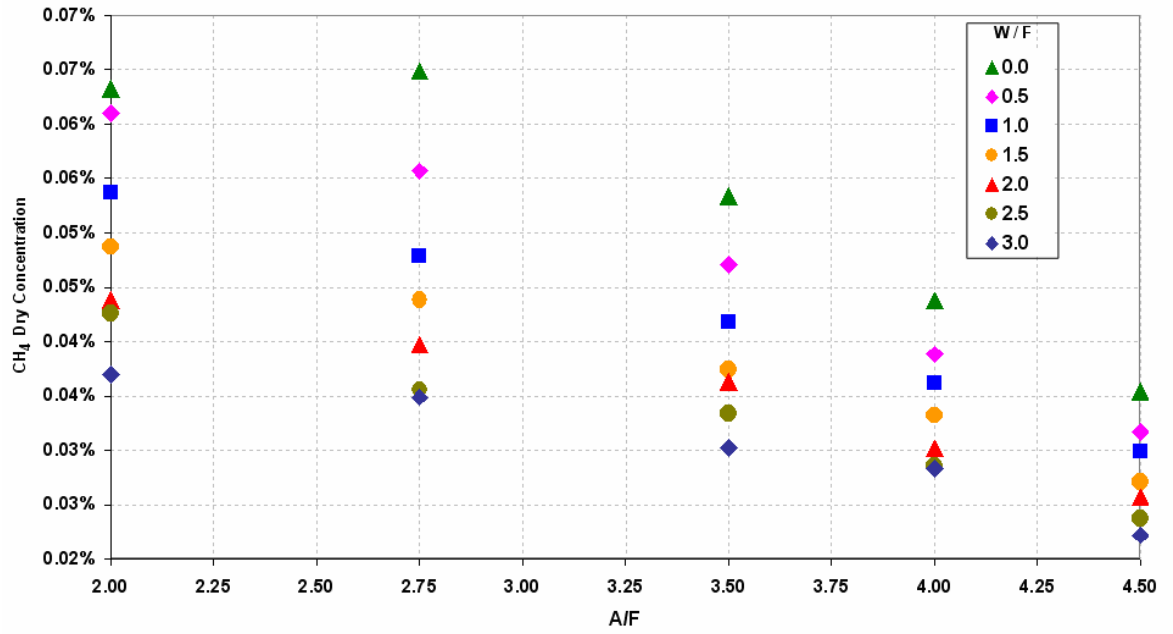

Figure 5.17 Change of CH_4 (dry) output with feed ratio

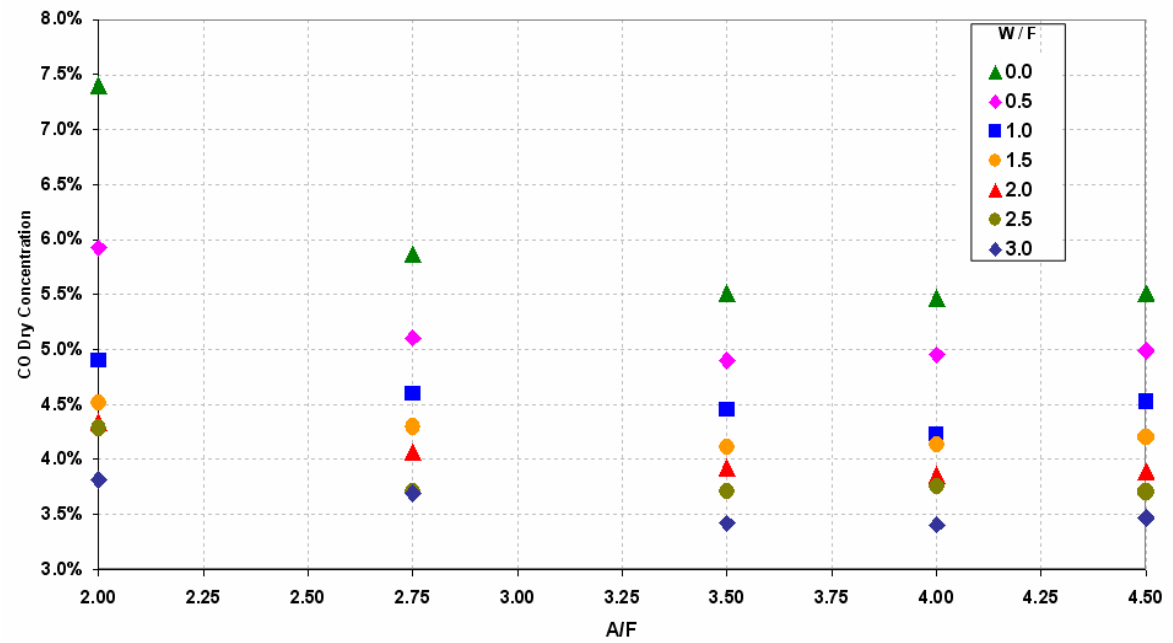

Figure 5.18 Change of CO (dry) output with feed ratio

The CH_4 concentration in product gas is almost linearly decreasing as the A/F ratio is increased. For the selected feed ratio range, the fuel concentration in product gas mixture is in the order of 10^{-4} %. On the other hand, CO concentration change in the product gas is not sensitive to the A/F ratio but, decreases dramatically as the W/F ratio is increased.

The overall fuel conversion efficiency can be seen in Figure 5.19 where the efficiency has been calculated as the H_2 obtained per mole of CH_4 fed. As it can be seen, with increasing A/F ratio, efficiency dramatically increases.

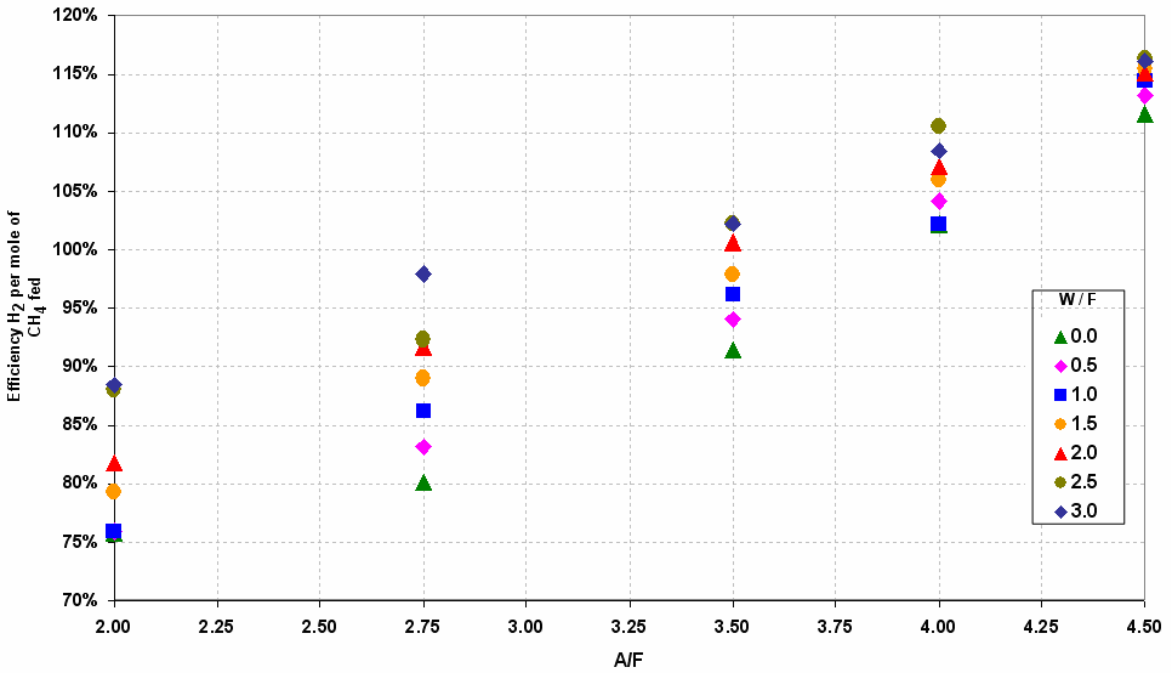

Figure 5.19 Fuel Conversion Efficiency

5.5. Effect of Catalyst Surfaces

5.5.1. The Surface Area of Catalysts

Figure 5.20 shows the molar concentrations of species in outlet stream and Figure 5.21 the resultant efficiency for different lengths of catalyst depositions where both oxidation and steam reforming catalyst surfaces are increased at the same time. The results are for inlet conditions A/F 3.5 and W/F 1.5.

According to the results, although the outlet CO concentration is decreased, increasing the catalyst surface had a negative effect on H_2 concentration as well as efficiency. This is because; the limiting condition for the given feed ratio is the consumption of fuel in the oxidation reaction. As the surface of Pt/δ-Al_2O_3 catalyst which is active for the oxidation reaction is increased, the amount of fuel consumed during oxidation increases, which in turn results in a decreased reactant concentration for the steam reforming reactions. So, the H_2 output and efficiency of the reformer decrease.

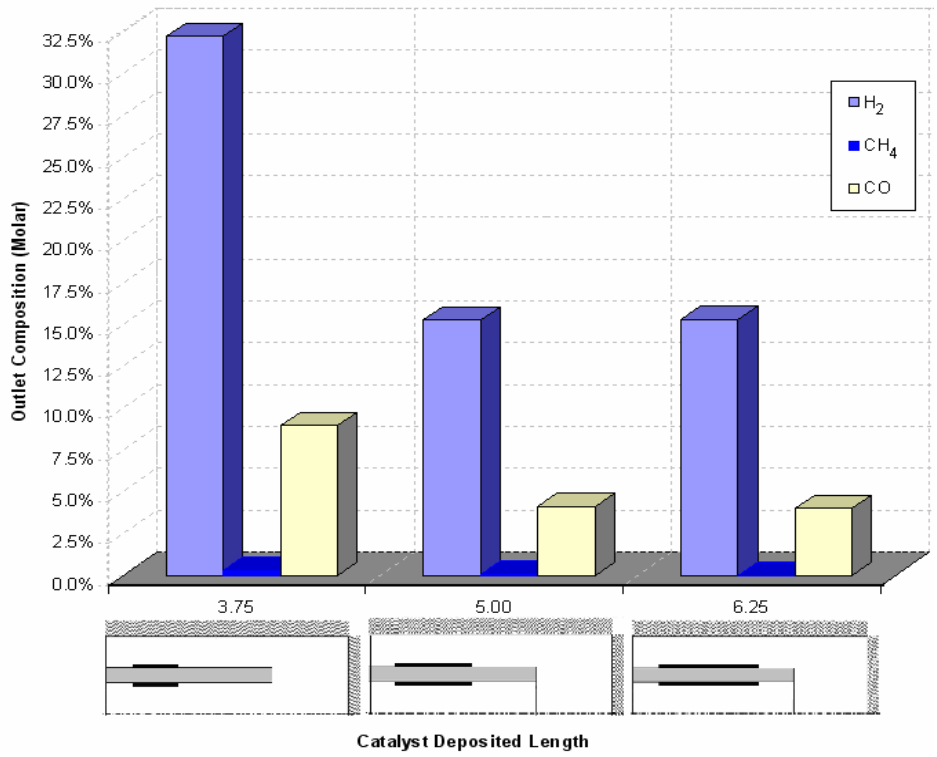

Figure 5.20 Effect of Catalyst Deposition on Molar Concentrations when both catalysts are increased

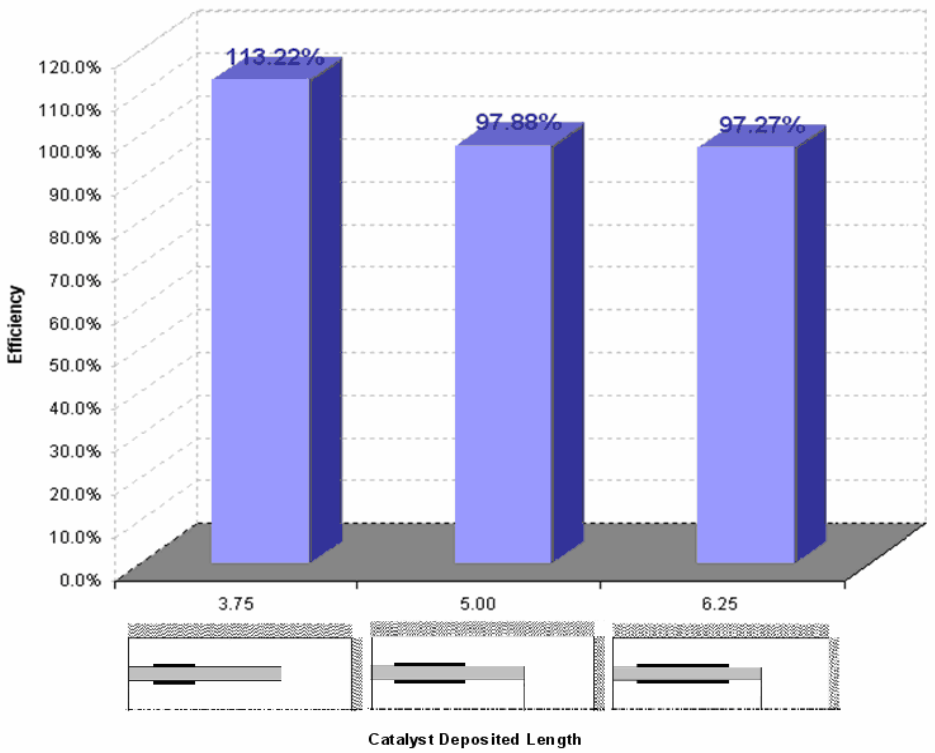

Figure 5.21 Effect of Catalyst Deposition on Efficiency when both catalysts are increased

Figure 5.22 and 5.23 show an alternative case, where for the same feed ratio, only the steam reforming catalyst surface is increased, while oxidation catalyst surface is kept at the initial length.

As can be seen, this time there is no decrease but a negligible increase in H_2 output as well as efficiency. Increasing the steam reforming catalyst surface could not have a significant effect on output since this time heat and H_2O supply limits the steam reforming reactions.

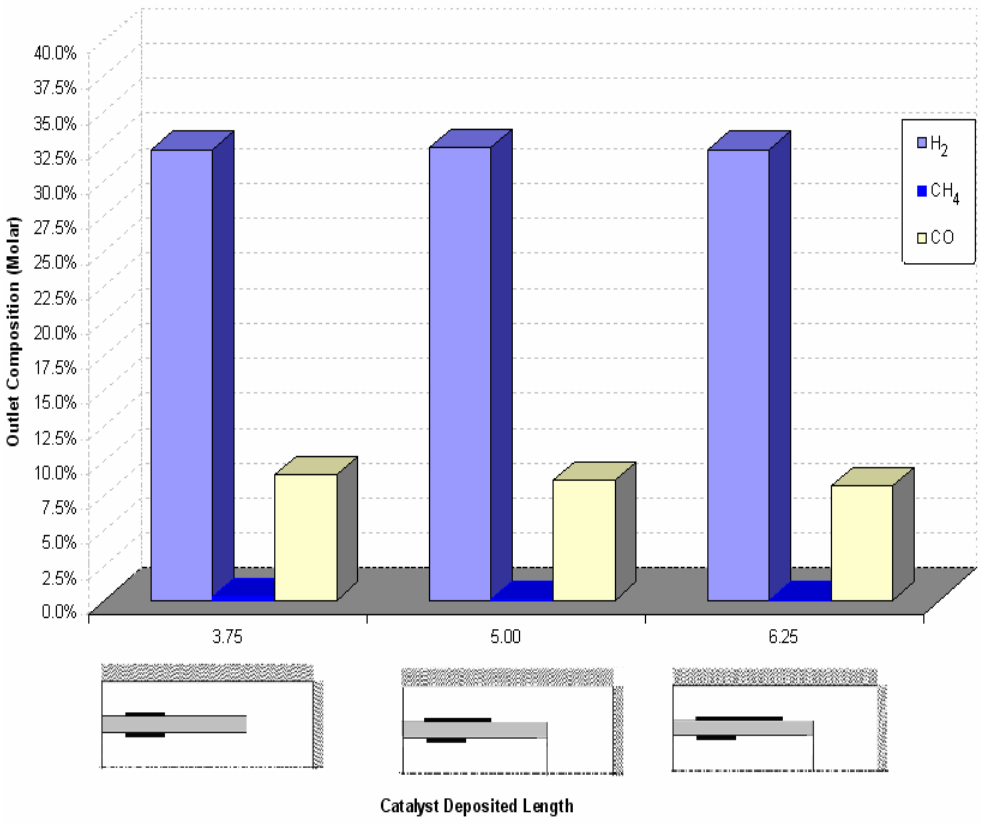

Figure 5.22 Effect of Catalyst Deposition on Molar Concentrations when only steam reforming catalyst is increased

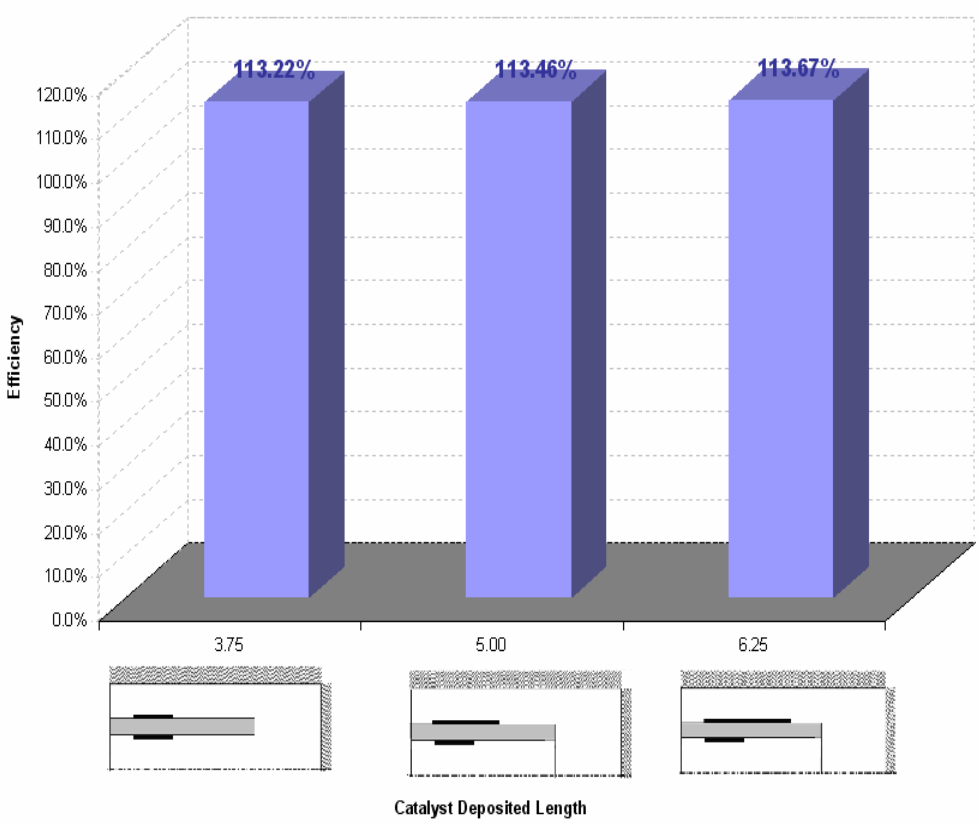

Figure 5.23 Effect of Catalyst Deposition on Efficiency when only steam reforming catalyst is increased

5.5.2. Relative Positions of the Catalysts

In order to see the effect of relative catalyst positions, four different cases were selected, where the oxidation catalyst is kept at a position while the steam reforming catalyst is moved from left to right.

Figure 5.24 shows the outlet concentrations together, 5.25 through 5.27 show each species in detail and Figure 5.28 shows the efficiency.

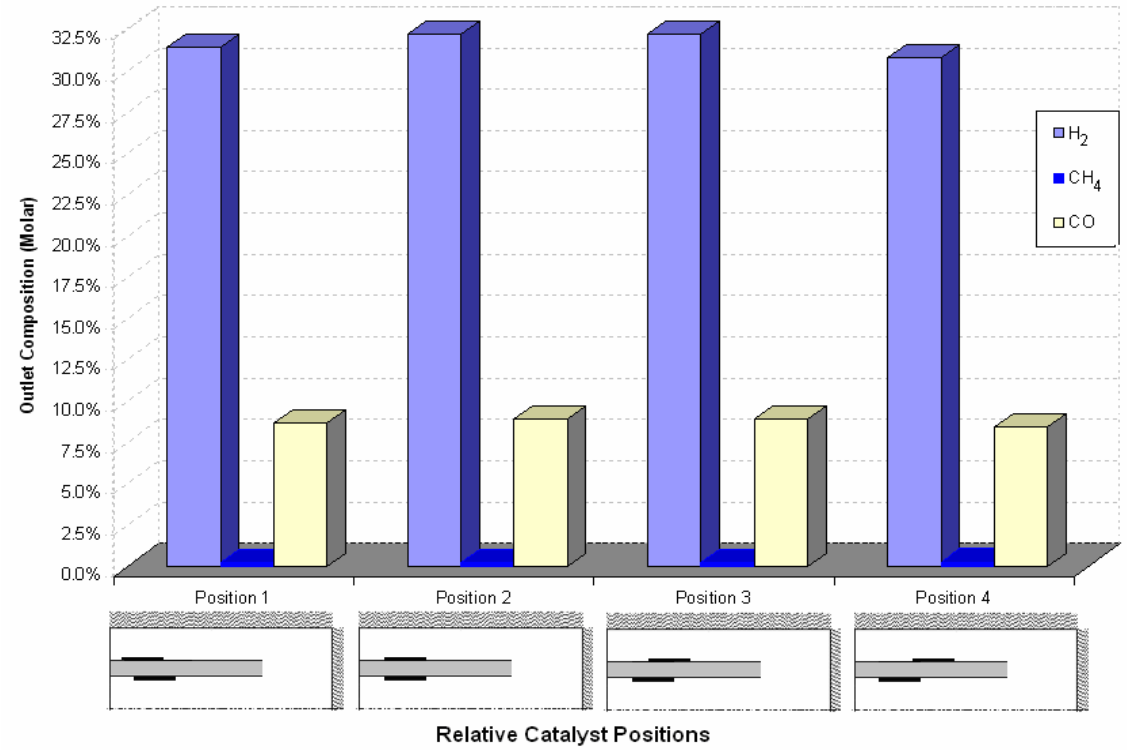

Figure 5.24 Effect of Relative Catalyst Positions on Molar Concentrations

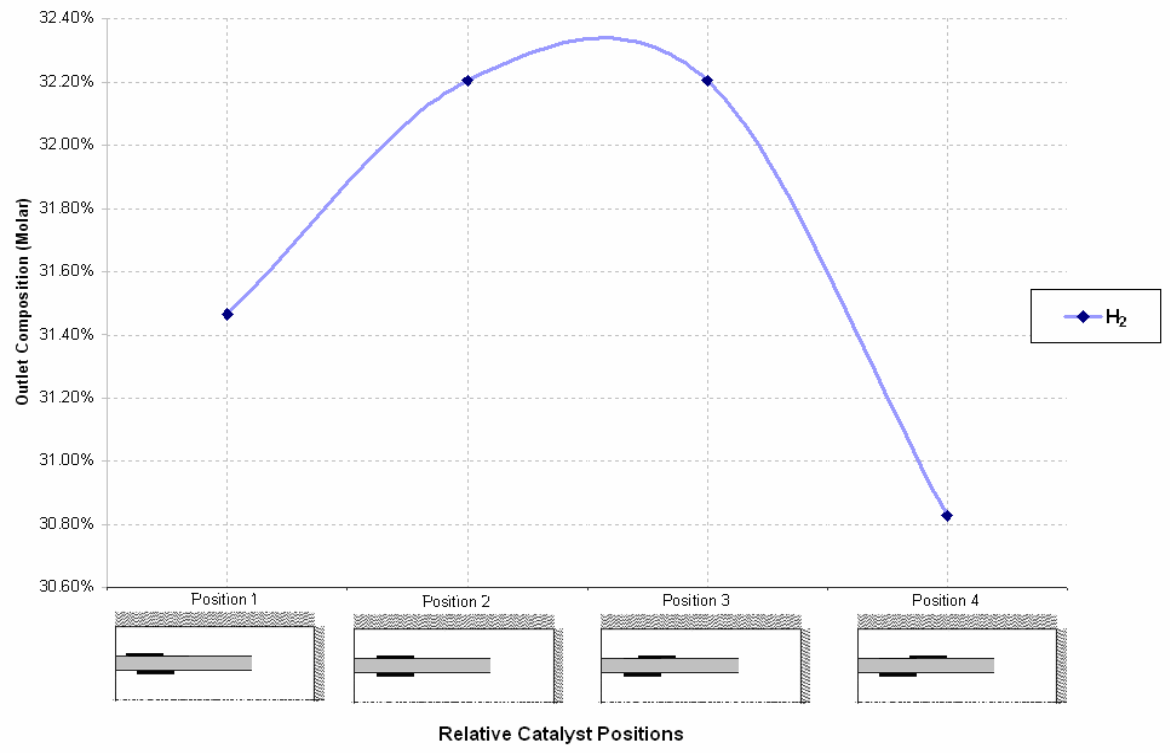

Figure 5.25 Effect of Relative Catalyst Positions on H_2 Concentration

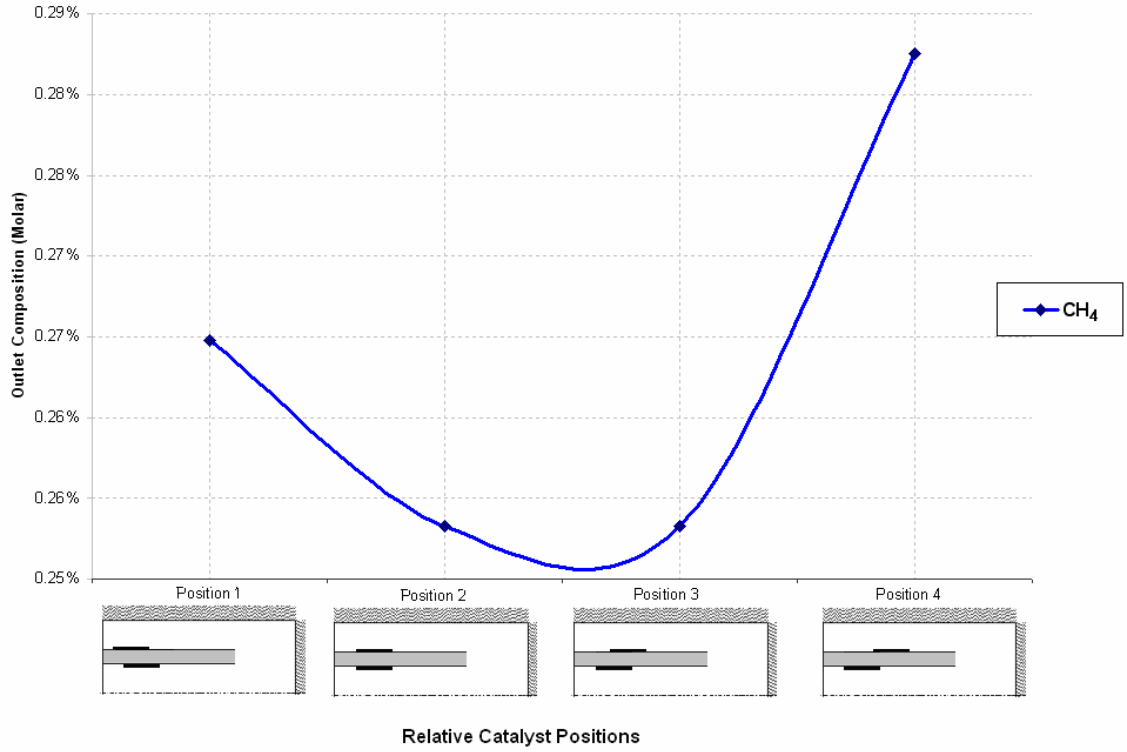

Figure 5.26 Effect of Relative Catalyst Positions on Residual Fuel Concentration

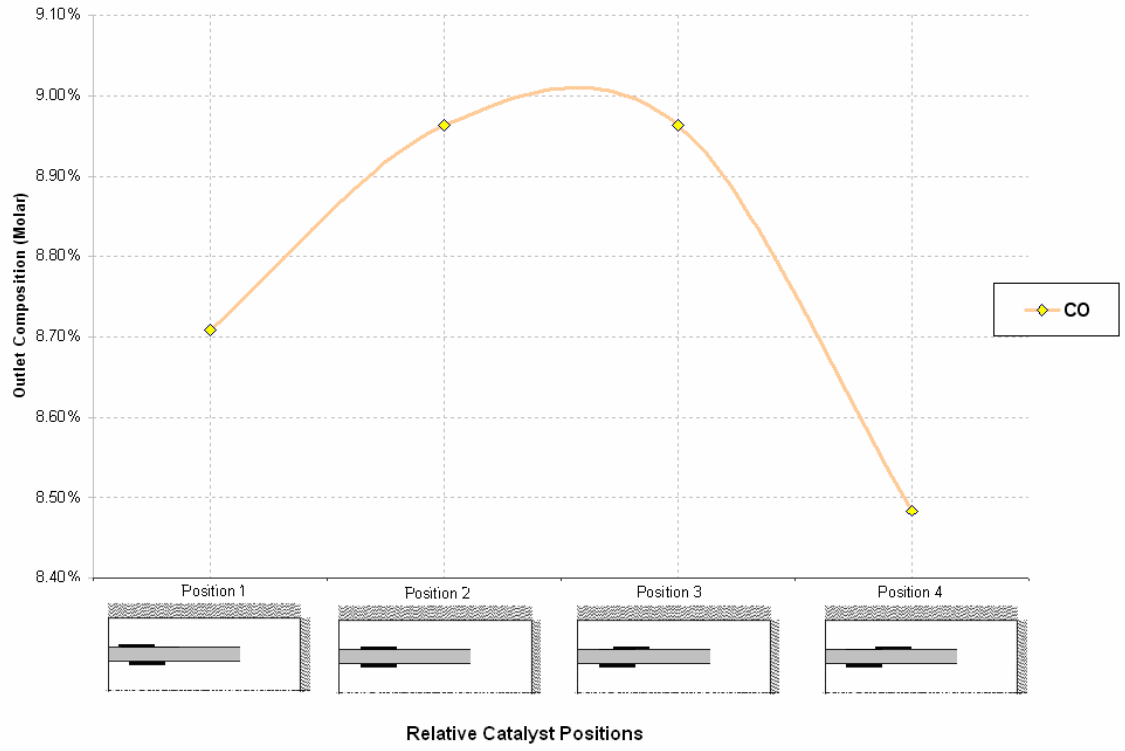

Figure 5.27 Effect of Relative Catalyst Positions on Residual CO Concentration

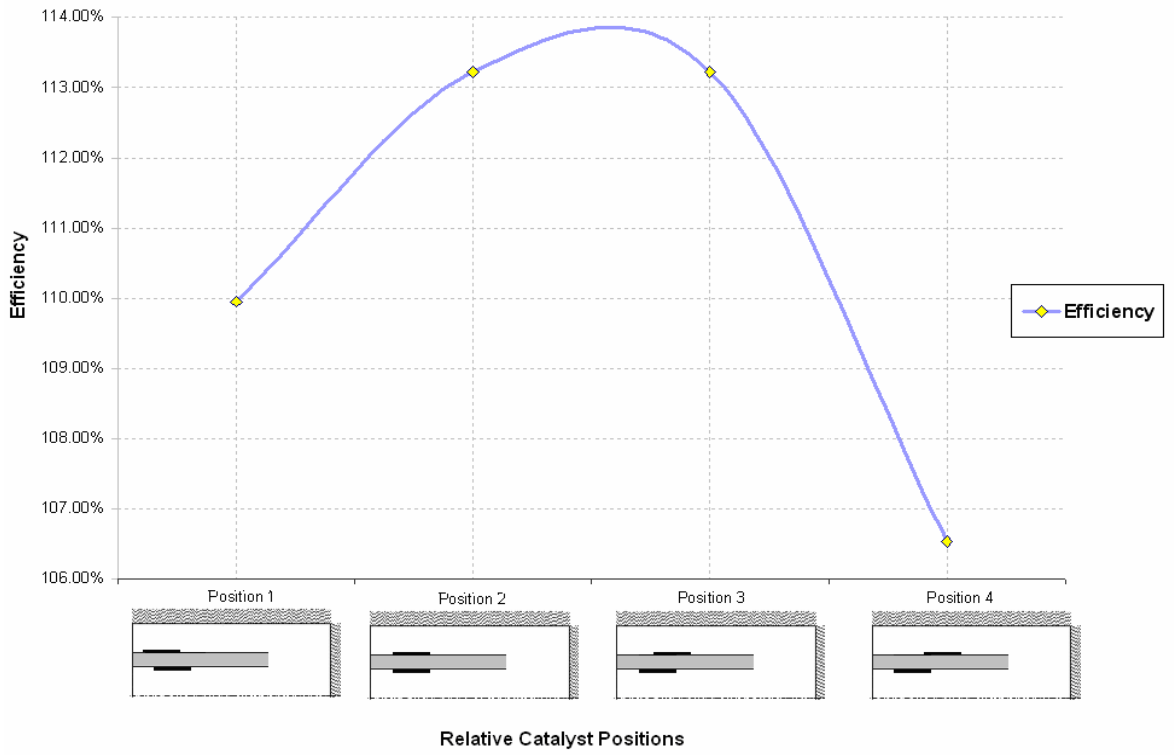

Figure 5.28 Effect of Relative Catalyst Positions on Efficiency

As the catalyst surfaces are moved apart from each other, H_2 output and efficiency decrease, the residual CH_4 in the outlet mixture increases, while CO is decreasing. The reason why moving the catalysts apart affects the reformer performance badly but CO removal positively is that, relatively weak heat transfer from combustion region to the steam reforming catalyst affects the steam reforming reaction negatively, but since water-gas shift reaction is not sensitive to the heat supplied, the more readily available H_2O favors the CO removal process.

6. CONCLUSIONS AND RECOMMENDATIONS

6.1. Conclusions

The major objective of this research was to simulate the performance of an autothermal heat-integrated wall reactor for hydrogen production by computer based modeling. The reactor model is analyzed for methane reforming and effects of certain parameters like air-to-fuel and steam-to-fuel ratio in inlet stream, and amount and configuration of the catalyst surfaces were investigated.

The results indicate that as the air-to-fuel ratio in the inlet stream is increased from 2.00 to 3.50, dry H_2 concentration shows a rapid decrease while after 3.50 increasing A/F ratio has no important effect on the amount of H_2 obtained. The same behavior is observed for CO left in the outlet stream. However, increasing the A/F decreases the amount of residual fuel (CH_4) in the outlet stream more rapidly as the amount of air is increased. As a result, conversion efficiency based on mole of hydrogen obtained per mole of fuel fed, increases with increased A/F ratio. Increasing A/F ratio from 2.00 to 4.50 results in an increase in the efficiency in the range of 28% to 39% for different water-to-fuel ratios.

Increasing the water-to-fuel ratio in the inlet stream from 0.0 to 3.0 causes a decrease in the outlet H_2 concentration. The effect is more dominant at low air-to-fuel ratios. Similar trend is observed for CH_4 and CO concentrations. Increasing W/F ratio from 0.00 to 3.00 results in an increase in the efficiency but effect is not strong as increased A/F ratio does. Increase in the efficiency is between 5% and 18% for different air-to-fuel ratios. Based on conversion efficiency, the optimum operating point is found out to be at air-to-fuel ratio 4.50 and water-to-fuel ratio 2.5.

Increasing both catalyst surfaces along the reformer axis from 37.5 % of the separating wall length to 50.0% causes a dramatic drop in H_2, CO and CH_4 concentrations in the outlet stream as well as efficiency. Increasing the surfaces more to 62.5 % of the wall length has no effect on H_2 and CO concentrations and efficiency, but decreases the residual amount of CH_4. If only the steam reforming catalyst surface is increased, no such

drop is observed except for CH_4. The highest conversion efficiency is reached when the oxidation catalyst was deposited over 37.5 % while the steam reforming over 62.5 % of the wall length. For the same inlet conditions, changing the catalyst surfaces increased the conversion efficiency from 97.9 % to 113.6 %.

It has been observed that the placement of the catalyst surfaces with respect to each other also has a strong effect on reactor performance. As the catalyst surfaces are placed apart from each other on the relative sides of the separating wall, conversion efficiency exhibits a drop from 113.2 % to 106.5 %.

6.2. Recommendations

Under the light of the results of this study, future work is needed to determine the effect of varying feed flow rate. Feed flow rate will have a critical effect on formation of hot spots as well as overall reactor performance.

In addition, increasing the reactor length and diameter will have an effect on the results as well as it will allow trial of more catalyst configurations.

7. REFERENCES

Ahmed S. and Krumpelt M., 2001, *Hydrogen from hydrocarbon fuels for fuel cells*, Int. Journal of Hydrogen Energy, 26, 291-301.

Andersen D.A., Tannehill J.C. and Pletcher R.H., 1984, *Computational Fluid Mechanics and Heat Transfer*, Taylor & Francis

Avcı, A.K., Önsan Z.İ. and Trimm, D.L., 2001, *On-board fuel conversion for hydrogen fuel cells: comparison of different fuels by computer simulations*, Applied Catalysis A: General 216, 243-256

Avcı, A.K., Önsan Z.İ. and Trimm, D.L., 2003, *On-board hydrogen generation for fuel cells powered vehicles: use of methanol and propane*, Topics in Catalysis, 22, 3-4

Avcı, A.K., 2003, *Computational and Experimental Investigation of Catalytic Hydrocarbon Fuel Processing for Autothermal Hydrogen Production*, PhD Thesis, Graduate Program in Chemical Engineering, Boğaziçi University

Avcı, A.K., Trimm, D.L. and Önsan Z.İ., 2001, Heterogeneous *reactor modeling for simulation of catalytic oxidation and steam reforming of methane*, Chemical Engineering Science, 56,641-649

Basile F., Fornasari G., Trifiro F. and Vaccari A., 2001, *Partial oxidation of methane Effect of reaction parameters and catalyst composition on the thermal profile and heat distribution*, Catalysis Today, 64, 21-30

Bird R.B., Stewart W.E. and Lightfoot E.N., 1960, *Transport Phenomena*, John Wiley and Sons, New York, p.258

Burmeister L.C., 1993, *Convective Heat Transfer*, John Wiley and Sons

Carroni R, Griffin T., Mantzaras J. and Reinke M., 2003, *High-pressure experiments and modeling of methane/air catalytic combustion for power-generation applications*, Catalysis Today, 83, 157-170.

Dillon A.C., Gilbert K.E.H., Parilla P.A., Horbacewicz C., Alleman J.L., Jones K.M. and Heben M.J. , 2003, *Hydrogen Storage in Carbon Single-wall Nanotubes, Hydrogen, Fuel Cells, and Infrastructure Technologies*, FY 2003 Progress Report

Dogwiler U., Benz P. and Mantzaras J., *Two-Dimensional Modeling for Catalytically Stabilized Combustion of a Lean Methane-Air Mixture with Elementary Homogeneous and Heterogeneous Chemical Reactions*, Paul Scherrer Institute, Combustion Research, CH-5232 Villigen-PSI, Switzerland.

Ersöz A., Olgun H., Özdoğan S., Güngör C., Akgün F. and Tırıs M., 2003, *Autothermal reforming as a hydrocarbon fuel processing option for PEM fuel cell*, Journal of Power Sources, 118, 384-392.

Frauhammer J., Eigenberger G., Hippel L.V. and Arntz D., 1999, *A new reactor concept for the endothermic high temperature reactions*, Chemical Engineering Science, 54, 3661-3670.

Freni S., Calogero G. and Cavallaro S., 2000, *Hydrogen production from methane through catalytic partial oxidation reactions*, Journal of Power Sources, 87, 28-38.

Geankopolis C.J., 1993, *Transport Processes and Unit Operations*, 3rd. Ed. Prentice Hall, New Jersey & Perry R.H., Green D.W., Maloney J.O., 1984, Chemical Engineer's Handbook, 6th ed., McGraw-Hill, Singapore

Groote A.M. and Froment G.F., 1996, Simula*tion of the catalytic partial oxidation of methane to synthesis gas*, Applied Catalysis A. General 136, 245-264.

Haydock H., (Secretary to the IEA Advanced Fuel Cells Executive Committee), 1998, *Introduction to Fuel Cells*, Technology-specific input to the CERT Ministerial Paper. November 1998.

Hirschfelder, J. O., Curtiss, C. F., and Bird, R. B., 1954, "*Molecular Theory of Gases and Liquids*," John Wiley and Sons, Inc., New York

Hoang D.L. and Chan S.H., 2004, *Modeling of a catalytic autothermal methane reformer for fuel cell applications*, Applied Catalysis A: General 268, 207–216.

Ioannides T. and Verykios X.E., 1998, *Development of a novel heat-integrated wall reactor for the partial oxidation of methane to synthesis gas*, Catalysis Today, 46, 71-81

Kee R.J., Dixon-Lewis G., Warnatz J., Coltrin M.E. and Miller J.A., 1996, *A Fortran computer code package for the evaluation of gas-phase multicomponent transport properties*, Sandia Report SAND86-8246, Reprint.

Kee R. J., Rupley F. M., Miller J. A., Coltrin M. E., Grcar J. F., Meeks E., Moffat H.K., Lutz A. E., Dixon-Lewis G., Smooke M. D., Warnatz J., Evans G. H., Larson R. S., Mitchell R. E., Petzold L. R., Reynolds W. C., Caracotsios M., Stewart W. E., Glarborg P., Wang C., Adigun O., Houf W. G., Chou C. P., and Miller S. F., 2003, *Chemkin Collection*, Release 3.7.1, Reaction Design, Inc., San Diego, CA.

Kolios G., Frauhammer J. and Eigenberger G., (2000), *Autothermal fixed bed reactor concepts*, Chemical Engineering Science, 55, 5945-5967

Kolios G., Frauhammer J. and Eigenberger G., 2001, *A simplified procedure for the optimal design of autothermal reactors for endothermic high-temperature reactions*, Chemical Engineering Science, 56, 351-357

Kolios G., Frauhammer J. and Eigenberger G., 2002, *Efficient reactor concepts for coupling of endothermic and exothermic reactions*, Chemical Engineering Science, 57, 1505-1510.

Liffler D.G., Taylor K. and Mason D., 2003, *A light hydrocarbon fuel processor producing high purity hydrogen*, Journal of Power Sources, 117, 84-91.

Ma L., Trimm D.L. and Jian C., 1996, *The design and testing of an autothermal reactor for the conversion of light hydrocarbons to hydrogen I. The kinetics of the catalytic oxidation of light hydrocarbons*, Applied Catalysis A. General 138, 275-283.

Ma L. and Trimm D.L., 1996, *Alternative Catalyst bed configurations for the autothermic conversion of methane to hydrogen*, Applied Catalysis A: General 138, 265-273

Merewether E.A., 2003, *Alternative Sources of Energy— An Introduction to Fuel Cells*, U.S. Geological Survey Bulletin 2179 , Reston, Virginia.

Ogden J.M., 2001, Re*vıew Of Small Stationary Reformers for Hydrogen Production*, Report to the International Energy Agency

Pettersson J. and Hjortsberg H., 1999, *Hydrogen Storage Alternatives- a technological and economical assessment*, Volvo Teknisk Utweckling AB, KFB-Meddelande 1999:27

Praharso, 2003, *The autothermal reforming of artificial gasoline*, PhD Dissertation, University of New South Wales.

Raissi A., 2002, Te*chnoeconomic Analysis Of Area II Hydrogen Production - Part II Hydrogen from Ammonia and Ammonia-Borane Complex for Fuel Cell Applications*, Proceedings of the 2002 U.S. DOE Hydrogen Program Review NREL/CP-610-32405

Rosner D.E., 1986, *Transport Processes in Chemically Reacting Flow Systems*, Butterworth Pub.

Shadid J.N., Moffat H.K., Hutchinson S.A., Hennigan G.L., Devine K.D. and Salinger A.G., 1996, *MPSalsa A Finite Element Computer Program for Reacting Flow Problems Part 1- Theoretical Development*, SANDIA REPORT SAND95-2752 c UC-4O5.

Song C., 2003, *Overview of Hydrogen Production Options for Hydrogen Energy Development, Fuel-Cell Fuel Processing and Mitigation of CO2 Emissions*, Proc. 20th International Pittsburgh Coal Conference, Sept 15-19, 2003, Pittsburgh, PA, USA Paper No. 40-3 (Hydrogen from Coal)

Paul, P.H., 1997, DRFM: *A new package for the evaluation of Gas Phase Transport Properties*, Sandia Report, SAND98-8203.

Williams, F. A., 1985, *Combustion Theory*, Benjamin/Cummings, Menlo Park, CA.

Xu J. and Froment G.F., 1989, *Methane Steam Reforming, Methanation and Water-Gas Shift: I. Intrinsic Kinetics*, AIChE J. 35, 88–96.